Deformation behavior of nano-precipitate strengthened materials in small dimensions

written by

Christina Hofer

ACKNOWLEDGEMENT

First of all I want to thank the ‘Marshallplan-Jubilaeumsstiftung’ for providing the financial support to perform my diploma thesis in the USA. The time at the University of California, Berkeley, was rewarding on both counts, professionally and personally.

My sincere gratitude and appreciation is due to my supervisor Dipl. Ing. Dr. mont. Peter Hosemann who not only guided me in my research but also integrated me in leisure time activities. I especially want to thank Dipl. Ing. Dr. mont. Erich Stergar for his great support and the fun we had during and besides work. Thank you for your endless patience and kindness. It was a pleasure working with the two of you.

Thank you to Dipl. Ing. Dr. mont. Harald Leitner for his encouragement to go abroad, inspiring discussions and the correction of this work.

My thanks are due to all colleagues of the Department of Nuclear Engineering at UC Berkeley and the Department of Physical Metallurgy and Materials Testing at the University of Leoben for supporting me in my experimentations.

Furthermore, I would like to thank my friends, especially Karoline Kormout without whom I could not have made it that far.

Finally I want to thank my parents for their unconditional support and strong faith in me during my studies.

Table of contents

Table of contents ..... **I**
List of figures ..... **III**
List of tables ..... **V**

1. Introduction **1**
2. Theoretical background **2**
2.1. Investigated material 2
2.2. Irradiation of structural materials 3
2.3. Nanoindentation 5
2.3.1. Basic principles 5
2.3.2. Data analysis 6
2.3.3. Corrections 9
2.4. Atom probe tomography 10
3. Experimental **12**
3.1 Specimen preparation for the irradiation 12
3.2. Calculation of parameters for the irradiation with SRIM 2008 12
3.3. Sample irradiation 14
3.4. Nanoindentation 16
3.5. Atom probe tomography 18
3.6. Micro-compression testing 19
4. Results **22**
4.2. Optical microscopy 22
4.3. Nanoindentation 22
4.3.1. Solution annealed condition 22
4.3.2. Aged condition 24
4.4. Atom probe tomography 24
4.4.1. Solution annealed condition 24

4.4.2. Solution annealed and irradiated condition 25
4.4.3. Aged condition 28
4.4.4. Aged and irradiated condition 32
4.5. Micro-compression testing 36
5. Discussion 41
5.2. Solution annealed condition 41
5.2.1. Aging at 500°C 41
5.2.2. Irradiation 42
5.3. Aged condition 46
6. Summary 47

References VI

List of figures

Figure 1. Heat treatment of precipitation hardened alloys (4). 2
Figure 2. Vickers pyramid on the left side and a Berkovich indenter on the right side (11). 5
Figure 3. (a) Typical force vs. time cycle of nanoindentation measurements. (b) Load-displacement data obtain during one cycle of loading and unloading (after (11)). 6
Figure 4. A schematic representation of a section through an indentation showing various quantities used in the analysis (13). 7
Figure 5. Indenter tip blunting results in a distorted contact depth h_c, and therefore an error in the contact area (15). 9
Figure 6. Depth dependence of the hardness of (111) single crystal Cu. Indentations of a minimum depth of 1.6 µm have to be performed to obtain the intrinsic hardness of 0.581 GPa (17). 10
Figure 7. Schematic diagram of a local electrode atom probe (LEAP) (18). 11
Figure 8. The number of displaced atoms in a cascade as a function of the PKA energy according to the model of Kinchin and Pease (9). 13
Figure 9. Schematic diagram of a tandem accelerator (after (22)). 15
Figure 10. (a) Sample mounting in the ion beam irradiation experiment (23). (b) Tandem ion accelerator at IBML in LANL (21). 15
Figure 11. Dose rate over depth profile calculated using SRIM 2008. 16
Figure 12. Schematic diagram of Micro Materials NanoTest™ (24). 17
Figure 13. A scanning electron micrograph of one array of indents on the sample aged for 2 h at 500°C. 18
Figure 14. FIB-based manufacturing of an atom probe needle. (a) Fabrication of a blank of 25 µm x 5 µm x 15 µm. (b) - (d) Cutting one strip of the foil and welding it to a sample stub on the multi-tip array. (e) – (f) Alternatively the entire foil can be transported to the multi-tip array and then cut into pieces. (g) The final sharp needle (29). 19
Figure 15. Custom sample holder containing a miniature goniometer to ensure proper sample alignment (30). 20
Figure 16. Optical micrographs of (a) the solution annealed condition and (b) after aging for 2h at 500°C. 22
Figure 17. One line of indentations on the solution annealed sample. 23
Figure 18. Hardness measured with nanoindentation and the calculated damage profile over the distance from the edge. 23

Figure 19. Hardness profile over the distance from the edge on the aged sample. 24
Figure 20. Atom maps of Fe, Cr, Ni, Al and Si the solution annealed state. There are no segregations visible. 25
Figure 21. Atom probe maps of Fe, Cr, Si, Ni and Al of the solution annealed material after 2 dpa proton irradiation. 26
Figure 22. FD-Analysis of Fe, Cr, Ni and Al of the solution annealed sample. A decomposition of all phases is clearly evident. 26
Figure 23. Analysis box through a Ni-enriched zone. 27
Figure 24. Concentration profile of the region of interest marked in Figure 23. 28
Figure 25. Atom probe maps of Fe, Cr, Ni, Al and Si of the material after aging for 2 h at 500°C. 28
Figure 26. Cluster found by means of the cluster search algorithm in the material after aging for 2 h at 500°C. 29
Figure 27. Size distribution of the precipitates after 2 h of aging at 500°C. 30
Figure 28. Analysis box through one precipitate. 31
Figure 29. Concentration profile through one precipitate as indicated in Figure 28. 32
Figure 30. Atom maps of Fe, Cr, Ni, Al and Si after 2 h of aging at 500°C and 2 dpa proton irradiation. 32
Figure 31. Precipitates in the aged and irradiated sample resulting from the cluster search algorithm. 33
Figure 32. Size distribution of the precipitates in the aged and irradiated specimen. 33
Figure 33. Analysis box through one precipitate. 34
Figure 34. Concentration profile of the region of interest marked in Figure 33. 35
Figure 35. Proximity histogram of Fe, Cr, Ni, Al and Si for an isoconcentration threshold of 18 at% Ni+Al. The continuous lines corresponds to the unirradiated, the dotted line to irradiated material. 36
Figure 36. Pillar 2 in the unirradiated area (a) ante and (b) post testing and Pillar 1 in the irradiated area (c) ante and (d) post testing. 37
Figure 37. Stress-strain curves gained from micro-compression tests on PH 13-8 Mo in the solution annealed state on the not irradiated part. 38
Figure 38. Top view of the pillars in the irradiated area post testing. The red line indicates the interface to the epoxy cold mount. 39
Figure 39. Engineering stress-strain curves gained from micro-compression tests on the irradiated area of the solution annealed sample. 39
Figure 40. Vacancy and interstitial concentration plotted over the time for irradiation at room temperature and a high sink density (42). 43

List of tables

Table 1. Typical chemical composition of PH 13-8 Mo in wt% according to the data sheet of 2010. 12
Table 2. Parameters of the irradiation experiment. 14
Table 3. Results from X^2 statistics of the irradiated solution annealed state. 27
Table 4. Chemical composition in at% calculated with the cluster search algorithm for the aged sample. 31
Table 5. Chemical composition in at% calculated with the cluster search algorithm for the aged and irradiated sample. 34
Table 6. Dimensions of the micro-pillars, measured in the SEM. 37
Table 7. Compression strength of the micro pillars. 40
Table 8. Increase in yield strength due to irradiation on the solution annealed sample. 45

1. Introduction

The increasing use of nuclear technology also necessitates the research on materials suitable for nuclear applications. In order to improve the safety, reliability, and efficiency of nuclear facilities or to develop future applications, it is necessary to understand the processes occurring in the material during irradiation. Sample irradiation in reactors or spallation sources is expensive and time-consuming. Proton irradiation has proven to be an effective way to induce radiation defects in the material in a short time and without highly activating it (1). Although the comparison of the results is not straightforward, ion-beam irradiation has become a popular tool for academic research. Due to the low energy of the protons, the penetration depth is limited. Therefore, small scale testing methods e.g. nanoindentation and micro-compression testing as well as methods for accurate sample fabrication have been developed in recent years.

During irradiation a large number of point defects are generated in the material, which further evolve into larger defects leading to a change in microstructure, dislocation density, void formation or phase composition. The accumulation of these defects can be delayed or suppressed by providing a large number of defect sinks such as dislocations and interfaces (2).

In this work the maraging steel PH 13-8 Mo was selected due to its outstanding mechanical properties, excellent corrosion resistance and low swelling (3), (4). Moreover the martensitic matrix and the fine dispersed intermetallic precipitates act as defect sinks, what makes this steel a good candidate for nuclear applications. The influence of irradiation on the precipitation kinetics and changes in the mechanical properties was investigated based on examination of the solution annealed state and an aged condition. The changes in mechanical properties were followed by utilizing nanoindentation and micropillars. The micropillars were produced in a focused ion beam microscope (FIB) and subsequently tested in the nanoindenter using a flat-punch indentation tip. To gain more information about the microstructure atom probe tomography measurements (APT) have been conducted.

2. Theoretical background

2.1. Investigated material

Precipitation hardening has proven to be one of the most effective ways of increasing the strength of a material. The principle of a particle dispersion hindering dislocation movement has then been used in numerous alloy systems and has also led to the development of martensitic hardenable steels, so-called maraging steels. The term “maraging” refers to “martensite” and “aging” and is frequently used for precipitation-hardened Fe-Ni alloys. Due to the precipitation of fine, uniformly dispersed intermetallic precipitates maraging steels combine high strength with an acceptable level of ductility.

Precipitates develop during a special two-stage heat treatment: solution annealing followed by cooling to room temperature and subsequent aging (Figure 1). After the first step of the heat treatment, the structure consist of a soft, but heavily dislocated nickel-martensite with a lattice parameter of a_α=2.878 Å (5). During the following aging treatment at temperatures between 400° to 600°C small, finely dispersed precipitates emerge (5)- (6).

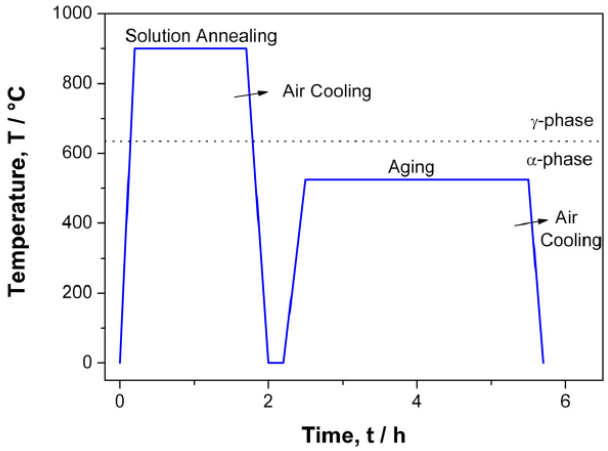

Figure 1. Heat treatment of precipitation-hardened alloys (7).

An addition of 13% Cr provides maraging steels with a good resistance for both general and stress corrosion cracking, making them suitable for many applications, such as extrusion dies, injection moulds and nuclear reactor components.

Most former investigations were carried out on overaged samples due to the inability of resolving the very fine precipitates at the early stages of aging with transmission electron microscopy (TEM). With the advent of atom probe tomography a deeper understanding of the evolution of the precipitates could be gained (8)- (9).

Guo et al. (8) reported that in PH 13-8 Mo NiAl-enriched zones with a composition far away from the stoichiometric β-NiAl phase are responsible for the increase in strength. The clusters emerge after short time and with persistent aging the amount of Ni and Al in the precipitates increases while the amount of Fe and Cr decreases. The precipitates are randomly distributed in the matrix and it appears that the precipitates emerge through homogeneous nucleation independent of lattice defects such as dislocations (10). Because the mismatch between the precipitates and the matrix is very low, the precipitates remain coherent even after long durations of aging (5).

Peak hardness is reached after 4 h of aging at 510°C, where the precipitation size accounts for 2-4 nm and their inter-particle distance is several nanometers (11). With prolonged aging the precipitates experience a classical coarsening process (9) and the chemical composition approaches the equilibrium NiAl-phase which has an ordered B2 (CsCl) superlattice structure (8), (11). Although the size of the precipitates increases with persistent aging, the precipitates are highly resistant to coarsening, allowing the alloy to keep the excellent properties during applications at elevated temperatures (8), (9).

The increase in strength due to aging is mainly attributed to NiAl order strengthening and the differences in the shear modulus of matrix and precipitates (5), (6). While (10) related the onset of hardening with the appearance of precipitation, Guo et al. (8) noticed an increase in hardness prior to precipitation which might be due to the redistribution of atoms, i.e. the solute segregation to dislocations.

2.2. Irradiation of structural materials

Radiation damage in structural materials and consequential changes in mechanical properties are a topic of major concern in designing systems operating in radiation environment. Understanding the processes occurring in the material during irradiation and the changes in microstructure is significant to prevent sudden failure of irradiated parts.

Radiation experiments in reactors are time-consuming, they lead to highly activated samples and they are therefore very costly. Proton irradiation has proven to be a very effective way to emulate the effects of neutron irradiation. Realizing a high dose rate at very short time without activating the sample is one of the substantial advantages of ion-beam irradiation. The main difference is the nature of the displacement cascade and the rate of damage accumulation. In principle, the conditions during proton irradiation can be controlled to arrive at a nearly identical microstructure and microchemistry as in the case of neutron irradiation (1). Although not all results can be compared directly to neutron experiments, it is a good way to gain basic information about the interaction of radiation and materials.

The radiation damage event is defined as the transfer of energy from incoming ions to lattice atoms in a collision. These lattice atoms are displaced of their original site, also travelling through the lattice displacing more atoms. Hence, each incident ion creates a collision cascade leading to a certain amount of vacancies and interstitial atoms.

The displacement of atoms is the fundamental process that drives the changes in structural materials which leads to a change in their properties (12):

- Radiation-induced hardening/ embrittlement
  The created point defects can accumulate to voids and dislocation loops or can enhance diffusion, allowing intermetallic precipitates to form. Hindrance of the movement of dislocations by these new obstacles causes radiation-induced hardening and, more important, embrittlement.
- Radiation-induced segregation
  The enhanced diffusion can also result in local segregation around grain boundaries. The enrichment of single elements on grain boundaries and the depletion around it is disadvantageous for the mechanical properties.
- Radiation-induced swelling
  Volume changes and swelling appear due to the formation of voids in the solid, thus, increasing the volume while the density of the material is decreased.
- Radiation-induced creep
  The physical changes also influence the mechanical response of a material when stress is applied. The increased amount of defects can cause phenomena such as radiation-induced creep, due to the enhanced ability of the dislocations to overcome obstacles.

In material science the damage due to radiation is measured in the unit displacements per atom (dpa), which means how often one atom has been displaced from its original lattice place.

2.3. Nanoindentation

2.3.1. Basic principles

Nanoindentation is a technique for measuring hardness and elastic modulus in small-scale. Mechanical properties can be determined directly from indentation load and displacement measurements without the need to image the hardness impression. The advantage of depth-sensing instruments is to keep error and time exposure small as well as the ability to obtain information about elastic and time-dependent plastic properties (13).

Indenters are typically made out of diamond, tungsten carbide, and sapphire and the most common geometries are Vickers (pyramidal with square base), Berkovich (pyramidal with triangular base), depicted in Figure 2, and spherical (14). A Berkovich indenter is more resistant to blunting due to his three-edge construction and has the same area-to-depth ratio as a Vickers indenter which makes the results of nano-tests comparable to micro-tests. Because Vickers hardness uses the area of the residual hardness impression and nanoindentation the contact area, the nanoindentation values need to be multiplied with 0.937 so both types of hardness share the same definition (15).

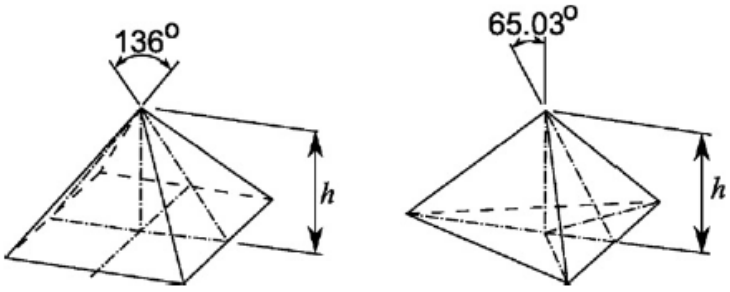

Figure 2. Vickers pyramid on the left side and a Berkovich indenter on the right side (14).

A typical force versus time cycle for indentation is shown in Figure 3a. After linear loading to the maximum force (a), it is held for a dwell period (b) to allow time-dependent plasticity or creep effects to diminish. Subsequently the specimen is unloaded to 10% of the maximum force (c) and held there for 60 s (d) to measure the thermal drift and then fully unloaded (e) (14).

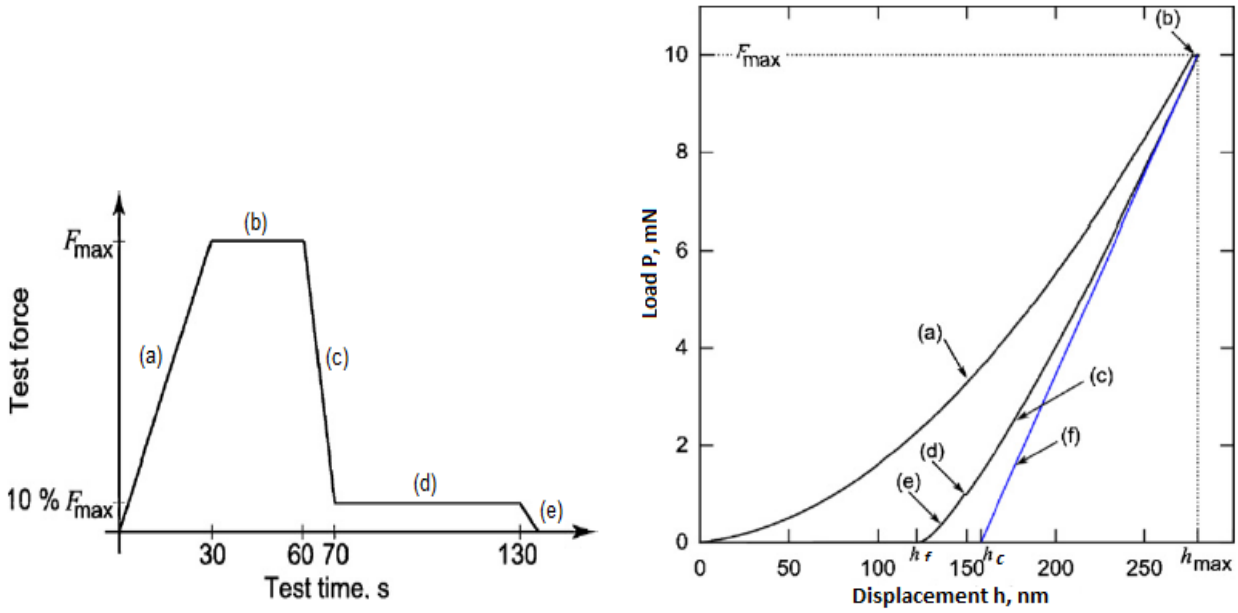

(a) (b)

Figure 3. (a) Typical force vs. time cycle of nanoindentation measurements. (b) Load-displacement data obtain during one cycle of loading and unloading (after (14)).

Load and displacement are continuously detected during the whole cycle leading to a data curve schematically depicted in Figure 3b. During loading elastic and plastic deformation occur, forming the residual hardness impression. It is assumed that only the elastic displacements recover during unloading and therefore the unloading curve displays the elastic properties (16).

2.3.2. Data analysis

When load is applied the indenter penetrates the surface to the maximum depth, h_{max}. It is assumed that the contact periphery sinks in around the indenter and thus, the contact depth h_c, along which contact is made between the indenter and the sample, is not the maximum depth:

$$h_c = h_{max} - h_s$$

After unloading an impression with the final depth h_f, remains as visible mark on the surface. Figure 4 shows a schematic representation of a section through an indentation (16).

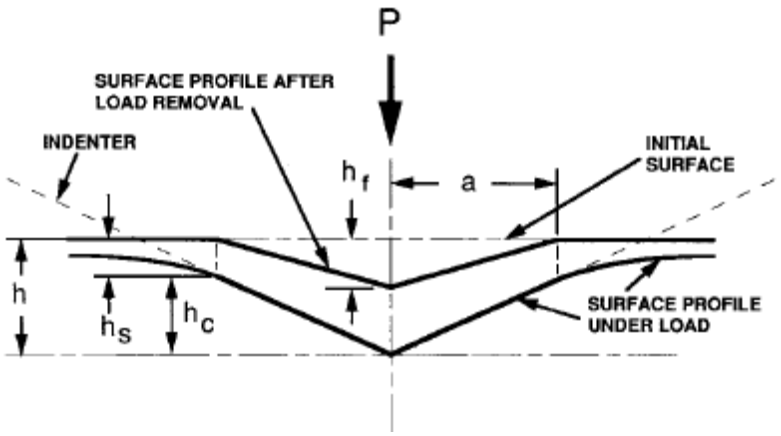

Figure 4. A schematic representation of a section through an indentation showing various quantities used in the analysis (16).

While conventional hardness measurements rely on direct imaging of the residual hardness impression, the error would be enormous using the same technique for nanoindentation. Therefore, the contact area under maximum load is calculated from the indenter shape and the contact depth:

$$A = F(h_c)$$

Awareness of the true contact area leads to the hardness, using the well-known equation:

$$H = \frac{Pmax}{A(h_c)}$$

The contact depth is not directly amenable in the load displacement curve but can be obtained by means of the contact stiffness *S*, defined as the slope of the unloading curve during the initial stage of unloading (blue line in Figure 3b):

$$h_c = h_{max} - \epsilon \frac{P_{max}}{S}$$

ϵ depends on the indenter shape and is 0.75 for a paraboloid of revolution.

There have been different approaches to measure the contact stiffness, which plays an important role in calculating the true contact area of the indenter and therefore is part of the equation for both hardness and Young's modulus. For a Berkovich indenter Doerner and Nix (17) suggested that the contact area does not change during the initial part of unloading and fitted a tangent to the top one-third of the unloading data. Extrapolating to zero load leads to the plastic depth h_0, used to calculate the contact stiffness with the following equation:

$$P = S(h - h_0)$$

Even though this method describes the behavior of most metals quite well, recovering during the initial stage of unloading is not taken into account. Hence, Oliver and Pharr (16) proposed to approximate the distinct curvature of the unloading curve by the power law relation:

$$P = \alpha(h - h_f)^m,$$

where α and m are power law fitting constants and h_f is the final depth. The initial unloading slope is then found by analytically differentiating this expression and evaluating the derivative at the peak load and displacement:

$$S = \frac{dP}{dh}$$

The reduced elastic modulus E_{eff}, which takes into account that elastic displacement does not only occur in the specimen but also in the indenter, follows from its relationship to contact area and measured unloading stiffness:

$$S = \beta \frac{2}{\sqrt{\pi}} E_{eff} \sqrt{A}$$

With the knowledge of Young's modulus E_i and Poisson's ratio ν_i of the indenter, the elastic constants of the specimen can be calculated:

$$\frac{1}{E_{eff}} = \frac{1 - \nu^2}{E} + \frac{1 - \nu_i{}^2}{E_i}$$

The Oliver and Pharr method (13) has established as standard method and will be used in all analyses of this work.

2.3.3. Corrections

To obtain reproducible results independent from environment and set-up some corrections need to be applied.

- For materials with distinctive time-dependent behavior the dwell period needs to be elongated to allow creep effects to diminish.
- It is best to wait until thermal equilibrium in the indentation chamber is established. Further changes in indentation depth from thermal expansion or contraction of the sample can be measured at a constant force and corrected afterwards (18).
- During indentation the observed indentation depth is a combination of sample penetration and bending of the frame. The frame compliance is a constant value for small forces, but is load-dependent for higher forces:

  $$h' = h - C_f P$$

  From the measured depth *h* the frame compliance C_f under the load *P* has to be subtracted to receive the corrected depth *h'* (18).
- Forming a hardness impression is associated with the movement of material. Depending on the ratio of the effective modulus to the yield stress, E_{eff}/σ_y, and the work-hardening behavior pile-ups may occur. Pile-ups result in an overestimation of the contact area, leading to similar errors in the hardness, and the modulus will be in error by a factor that scales as $\sqrt{A}$. Atomic force microscope examinations have to be conducted to measure the amount of pile-up (13).
- Another big influence on the obtained contact area is the indenter shape. In practice, it is not possible to manufacture a perfectly sharp indenter tip. Moreover with proceeding use the indenter blunts, distorting the contact depth h_c, and therefore the contact area (Figure 5).

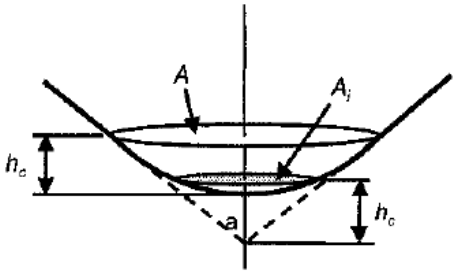

Figure 5. Indenter tip blunting results in a distorted contact depth h_c, and therefore an error in the contact area (18).

This error can be corrected by applying an area correction function which is obtained by performing indentations on a reference sample. The correction becomes less important with increasing indentation depth (18).

- The indentation size effect is a well-known phenomenon whereby the measured hardness values increase with decreasing load. De Guzman et al. (19) explained that behavior by the concept of geometrically necessary dislocations, which are the dislocations forming the residual hardness impression. At shallow penetration depths the density of dislocations underneath the indenter tip is very high yielding to a higher hardness value. This effect diminishes with increasing penetration depth and the hardness approaches the intrinsic value (19). Using this theory Nix and Gao (20) proposed a way to calculated the intrinsic hardness H_0 as well as the minimum depth h^* necessary for load-independent hardness measurements:

$$\frac{H}{H_0} = \sqrt{1 + \frac{h^*}{h}},$$

where H is the hardness for a given depth of indentation h.

Plotting the square of the hardness against the reciprocal of the depth leads to a straight line where the intercept is H_0 and the slope h^*, exemplarily depicted in Figure 6.

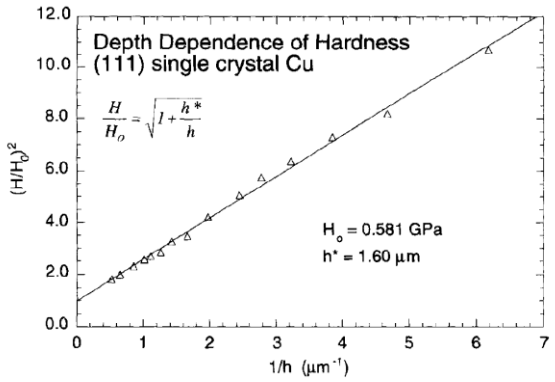

Figure 6. Depth dependence of the hardness of (111) single crystal Cu. Indentations of a minimum depth of 1.6 µm have to be performed to obtain the intrinsic hardness of 0.581 GPa (20).

2.4. Atom probe tomography

Atom probe tomography is a very suitable examination method for the early stages of precipitation. The combination of a time-of-flight mass spectrometer and a position-

sensitive detector allow a three-dimensional reconstruction of the investigated material with near-atomic resolution. Applying a high voltage to a needle-shaped specimen with a tip radius of about 50 nm creates a high electric field on the specimen's apex. Superimposing of the standing voltage with voltage pulses leads to field evaporation of the surface atoms. The chemical identification of the single atoms follows based on the mass-to-charge ratio $\frac{m}{n}$:

$$\frac{\mathrm{m}}{\mathrm{n}} = \frac{\mathrm{c}(\mathrm{V_{dc}} + \alpha \mathrm{V_{pulse}})\mathrm{t}^2}{\mathrm{d}^2}$$

C is a constant (c=1.93x10^{-4}) used to convert mass into atomic mass units, V_{dc} and V_{pulse} are standing and pulse voltage, *α* is the pulse amplitude coupling factor which accounts for some loss in the effectiveness of the pulse, *d* is the distance between specimen apex and detector and *t* is the time of flight, which results from the time between the evaporating pulse and the atom detection. The equal detection efficiency of all elements ensures a truthful reflection of the chemical composition.

The latest generation of atom probes is featured with a local electrode, as shown in Figure 7. The major benefit of the local electrode is the possibility of using multi-tip arrays because the evaporation field can be localized within a small region.

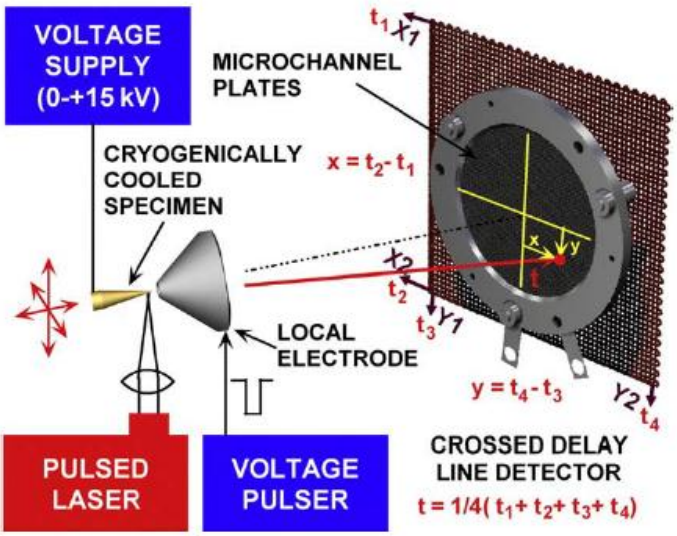

Figure 7. Schematic diagram of a local electrode atom probe (LEAP) (21).

A typical use of atom probe tomography is to visualize nanometer-sized precipitates and determine their size, shape, composition, number density and volume fraction.

3. Experimental

3.1 Specimen preparation for the irradiation

The investigated PH 13-8 Mo was commercially produced and provided by the company Uddeholm. The nominal chemical composition is given in Table 1. The alloy was delivered in the solution annealed condition (850°C, 0.5 h). Subsequently part of the material was aged at 500°C for 2 h.

Table 1. Typical chemical composition of PH 13-8 Mo in wt% according to the data sheet of 2010.

	Fe	C	Cr	Ni	Al	Mo	Mn	Si
PH 13-8 Mo	Bal.	0.03	12	9.2	1.6	1.4	0.3	0.3

Pieces of 10 mm x 10 mm x 2 mm of the solution annealed and the aged condition were grinded with Silicon metallurgical paper up to 1200 grit and polished with diamond suspension with a particle size of 3 and 1 µm at a Struers Rotopol-V. As the last step the samples were polished with 0.1 µm colloidal silica suspension for approximately 3 h on a Buehler VibroMet 2 polisher.

3.2. Calculation of parameters for the irradiation with SRIM 2008

The goal of the irradiation was to create a damage of 2 dpa. The resulting damage profiles and the beam parameters can be calculated by Monte Carlo methods, for example the SRIM (The Stopping of Range of Ions in Matter) code version 2008.04 (22). Necessary parameters for the calculation are:

- Type and energy of the incident particles
- Composition and density of the target material
- Displacement energy
- Beam current
- Size of the irradiated area

The radiation experiments were performed at the Ion Beam Material Laboratory (IBML) at the Los Alamos National Laboratory (LANL) using a 3.2 MV tandem ion accelerator.

The accelerated ions, in this case ionized hydrogen, hit the target with an energy of 1.3 MeV. The energy of the ions and the composition of the target (Table 1) determine penetration depth and extension of the radiation damaged zone. The incident ion impinges on a target atom, transfers parts of its kinetic energy and as a result the struck atom, also called a primary knock-on atom (PKA), is displaced of its original lattice site. The ion and the PKA travel through the lattice, creating additional knock-on atoms what leads to a displacement cascade. Kinchin and Pease (23) developed a model to calculate the amount of vacancies created by a PKA depending on its energy *T*. The result of their model is shown in Figure 8, where E_d is the displacement energy, the minimum energy a lattice atom must receive in a collision to be displaced from its site, and E_c is a cut-off energy above which no additional displacements occur until the PKA energy decreased to it.

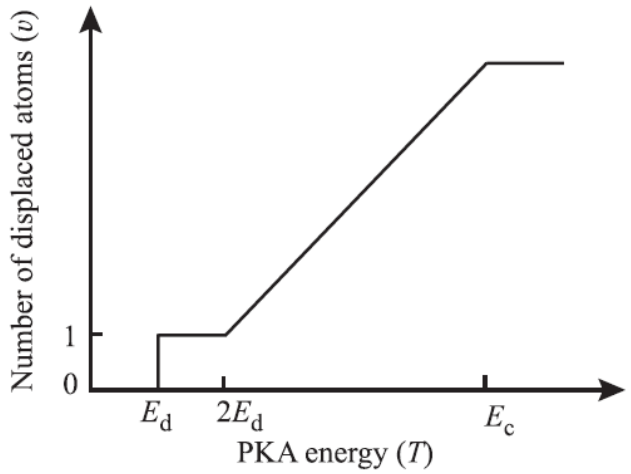

$$\nu(T) = \begin{cases} 0 & \text{for } T < E_d \\ 1 & \text{for } E_d < T < 2E_d \\ \dfrac{T}{2E_d} & \text{for } 2E_d < T < E_c \\ \dfrac{E_c}{2E_d} & \text{for } T \geq E_c \end{cases}$$

Figure 8. The number of displaced atoms in a cascade as a function of the PKA energy according to the model of Kinchin and Pease (12).

The displacement energy arises from the potential fields around the struck atom, which the atom has to pass in order to be displaced. The potential barrier is not equal in all direction. For simplification a single value, which represents a spherical average of the potential barrier surrounding the equilibrium lattice site, of 25 eV is given for the displacement energy (12). With this information the SRIM code calculates the damage rate *D*, the produced vacancies per incoming ion per angstrom:

$$D = \frac{vac}{ion * \text{Å}}$$

To get the damage in displacements per atom, the calculated damage profile was multiplied with the current density *j*, and the reciprocal of the atom density *ρ*:

$$D * j * \frac{1}{\rho} = dpa$$

The current density can be determined by measuring the current induced in the sample and the time the sample is exposed to the beam:

$$j = \frac{I}{A * t}$$

where *I* is the beam current, *A* the irradiated area on the sample and *t* the irradiation time. During irradiation the beam current was logged and the exposure time was adapted according to the desired dose. Table 2 summarizes the irradiation parameters.

Table 2. Parameters of the irradiation experiment.

Ion	Energy [keV]	Temperature [°C]	Current [µA]	Area [mm^2]	Time [h]	Depth [µm]	Dose [dpa]
H^+	1300	RT	~2.5	2.5x2	20	~10	2

3.3. Sample irradiation

The radiation experiments were performed at the Ion Beam Material Laboratory (IBML) at the Los Alamos National Laboratory (LANL) using a 3.2 MV tandem ion accelerator. A schematic diagram of the set-up and an image of the accelerator are depicted in Figure 9 and Figure 10b. The ions extracted from the ion source have an energy of 50 keV. A tandem accelerator consists of two accelerating tubes which are connected by a high voltage terminal. At the terminal a high positive voltage is applied accelerating the negative ions towards it. The ions pass through an electron stripper where the negative ions are converted into positive ones which are repelled by the terminal. At each step the ions were accelerated by 0.647 MeV, leading to a total energy of 1.344 MeV (24).

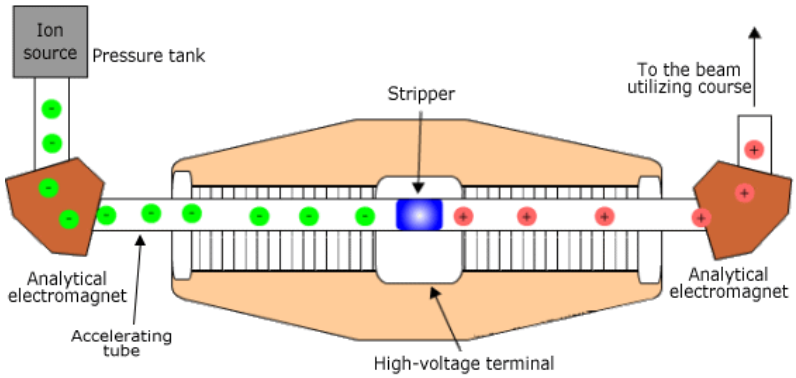

Figure 9. Schematic diagram of a tandem accelerator (after (25)).

Two samples at a time were mounted on a copper sample holder, shown in Figure 10a, using silver paste and carbon tape to ensure good adhesion and thermal conductivity to dissipate the induced heat. During the experiment the temperature was measured with a thermocouple which was located underneath the sample and the current induced in the sample was monitored.

(a) (b)

Figure 10. (a) Sample mounting in the ion beam irradiation experiment (26). (b) Tandem ion accelerator at IBML in LANL (24).

Figure 11 shows the calculated damage profile in dpa. The blue curve represents the amount of vacancies created in the material; the red curve illustrates the stopping range of the Hydrogen ions. The damage is nearly uniform through the first 8 μm of the total range of 10 μm, resulting in a damage of 2 dpa.

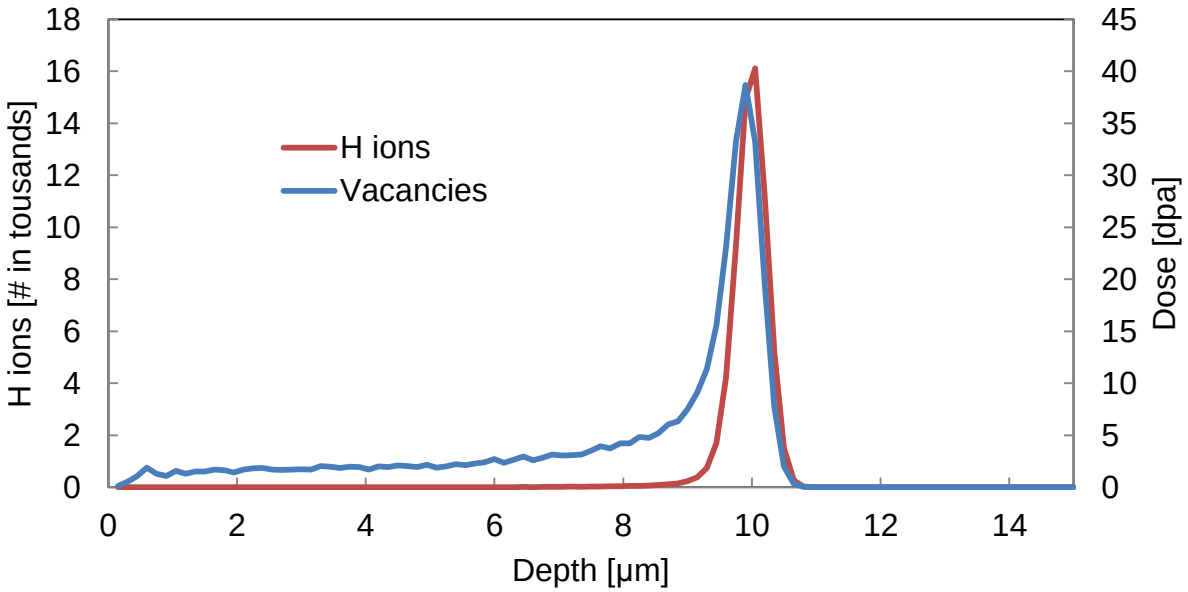

Figure 11. Dose rate over depth profile calculated using SRIM 2008.

3.4. Nanoindentation

After the irradiation the samples were embedded upright in epoxy cold mount to investigate the cross section. As the last step of the preparation the samples were polished with 0.1 µm colloidal silica on a Buehler vibromet polisher.

The nanoindentation measurements were conducted on the Micro Materials NanoTest™, schematically shown in Figure 12. The vertically system is based on a pendulum that can rotate on a friction-less pivot. On top of the pendulum a coil and a magnet are mounted. When current is applied the coil is attracted to the magnet and the indenter tip penetrates the surface of the specimen electromagnetically. The imposed force is controlled by varying the current in the coil. The indention depth is measure by means of a capacitor; one plate is attached to the diamond hold, changing therefore the capacity according to the depth of indentation (27).

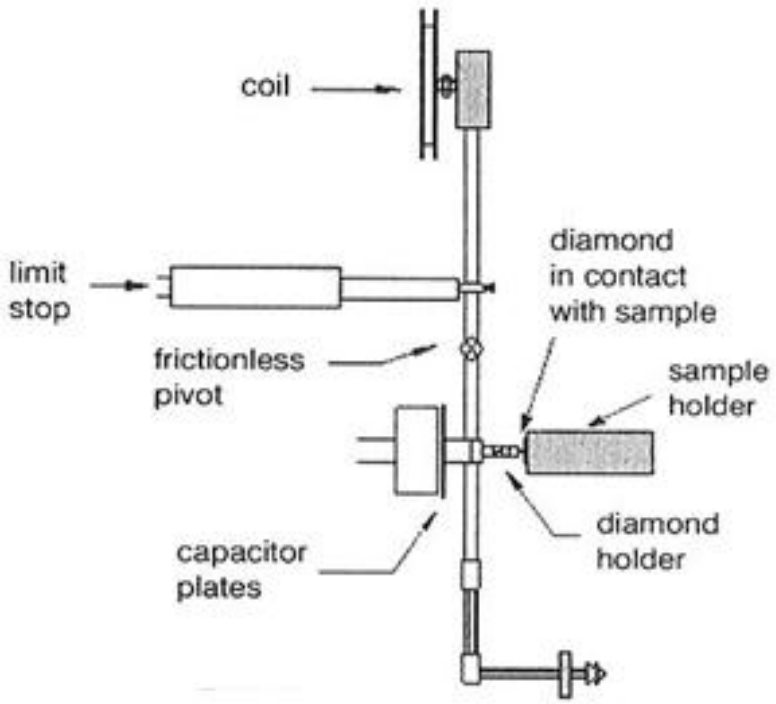

Figure 12. Schematic diagram of Micro Materials NanoTest™ (27).

A Berkovich diamond indenter tip was used to perform the nanoindentation measurements. Constant displacement mode was used for all indentations on the cross-section to ensure constant indentation depth. Moreover, it eliminates the influence of the indentation size effect in one array of indentations. Starting from the edge 5 rows with 20 indentations to a nominal depth of 200 nm were conducted. The rows were set in an angle of about 20° for better resolution. The indentations were 4 µm apart from each other, resulting in a grid of 100 indentations measuring as far as 25 µm away from the edge, as shown in Figure 13.

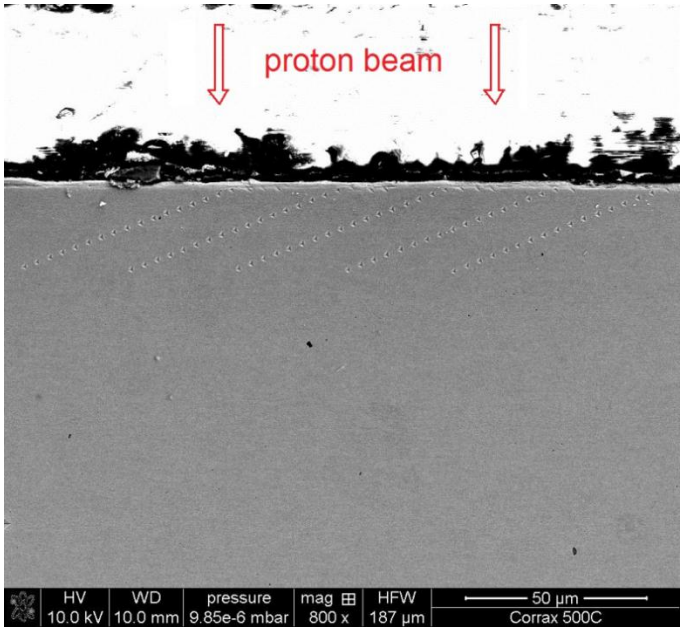

Figure 13. A scanning electron micrograph of one array of indentations on the sample aged for 2 h at 500°C.

3.5. Atom probe tomography

The ATP measurements were conducted at the Center for Advanced Energy Studies (CAES) in Idaho Falls, ID, USA. For all measurements a LEAP 4000X HR was used.

Usually needle-shaped specimens are fabricated by a standard two-step etching method (28). Since in this case material of a specific location was needed a FIB-based lift-out method was applied (29)- (30), as shown in Figure 14. First a protective platinum layer was deposited on top of the region of interest. Then two rectangular cross sections were trenched at a distance of about 2 µm were milled above and beyond the region of interest to receive a blank of 25 µm x 2 µm x 15 µm. The specimen was tilted 52° with respect to the ion beam to perform the undercut. Before the final side was cut free the blank was attached to the lift-out probe through platinum deposition. The blank remained on the lift-out probe while the bulk specimen was replaced by a multi-tip array. The end of the blank was attached with platinum deposit to a post on the array and subsequently cut free. This process was repeated with the rest of the material. Subsequently needle shaped samples with a circular cross-section, an end radius of about 50 nm, and a taper-angle below 5° were cut. The last step was a low voltage (2 kV) cleaning step to reduce the ion beam influenced region.

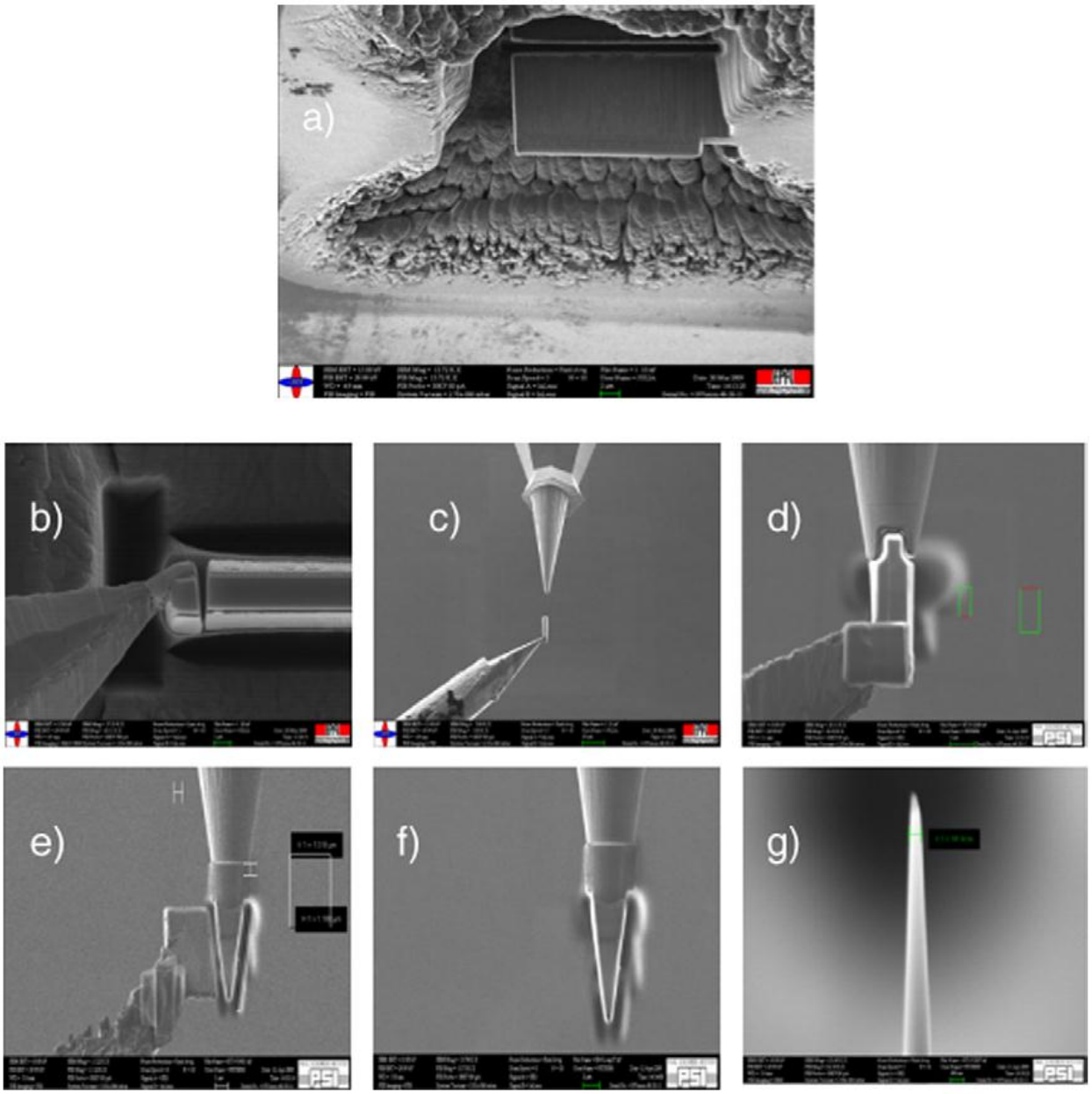

Figure 14. FIB-based manufacturing of an atom probe needle. (a) Fabrication of a blank of 25 µm x 2 µm x 15 µm. (b) - (d) Cutting one strip of the foil and welding it to a sample stub on the multi-tip array. (e) – (f) Alternatively the entire foil can be transported to the multi-tip array and then cut into pieces. (g) The final sharp needle (31).

The experiments were performed at a temperature of ~65 K in an ultrahigh vacuum (10^{-9} Pa) using a pulse fraction of 20% of the standing voltage. Data reconstruction and statistical evaluation were conducted using the software package IVAS^{TM} 3.6.0 from Cameca Science and Metrology Solutions.

3.6. Micro-compression testing

Uniaxial compression tests were performed on the solution annealed sample on the irradiated and the unirradiated area. The main benefit of micro-compression testing compared to nanoindentation is that no strain gradient is imposed. The pillars were machined with a FEI Quanta4000 FEG dual-beam focused ion microscope using Ga^+ ions with a kinetic energy of 30 keV. Rough cuts were performed at a current of 15 nA at an angle of 52°. It is necessary to mill an area large enough so that the flat-punch indentation tip of a diameter of 30 µm does not hit any surrounding material. Subsequently, the pillars have been shaped at an angle of 54° to mill away the visible taper of the sidewalls using a lower beam current (0.5-3 nA) to minimize re-deposition (32). The pillars in the irradiated zone were placed close to the edge to make sure the whole volume of the pillar suffered radiation damage.

The uniaxial compression experiments were performed on MicroMaterials NanoTest™ outfitted with a diamond flat-punch indentation tip. It is challenging to mount the flat-punch perpendicular to the sample surface and therefore ensure proper contact at the initial stage of the experiment. Contact misfit leads to smearing the transition from elastic-to-plastic flow as well as a lower measured modulus upon initial loading. As proposed by Uchic and Dimiduk (32) a custom sample holder containing a miniature goniometer was used for sample alignment, shown in Figure 15.

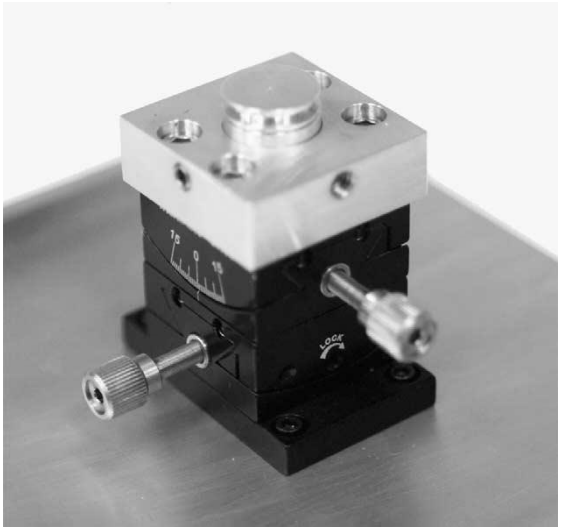

Figure 15. Custom sample holder containing a miniature goniometer to ensure proper sample alignment **(32)**.

The pillars were tested with a loading and unloading rate of 1 mN/sec using load-controlled mode.

The frame compliance, c_f=0.41464866, was applied according to (18):

$$h' = h - c_f * P$$

where *P* is the load, *h* the measured depth and *h'* the corrected depth.

It needs to be considered that compression not only occurs in the pillar but as well in the underlying material. Sneddon (33) analytically solved the problem of pushing a rigid punch into an infinite half-space. Supposing that the behavior of the underlying material can be approximated with this relationship, the column displacement can be calculated as suggested by Volkert and Lilleodden (34):

$$\Delta h = h' - \frac{(1-\nu^2)}{E} * \frac{F}{\frac{d_1+d_2}{2}}$$

where *E* and *v* are the elastic constants of the underlying material.

The obtained force-displacement curves were transformed into engineering stress-strain curves by

$$\sigma = \frac{F}{(d_1 * d_2)}$$

and

$$\epsilon = \frac{\Delta h}{h}$$

The dimensions of the pillars were obtained in the scanning electron microscope (SEM) prior to testing, where d_1 and d_2 are the diameters of the cross section area and *h* is the column height, defined as the vertical distance between the extrapolated intersections of the inclined walls and the top of the column.

4. Results

4.2. Optical microscopy

After the heat treatment all conditions were examined through optical microscopy. As expected, both samples are fully martensitic, as shown in Figure 16.

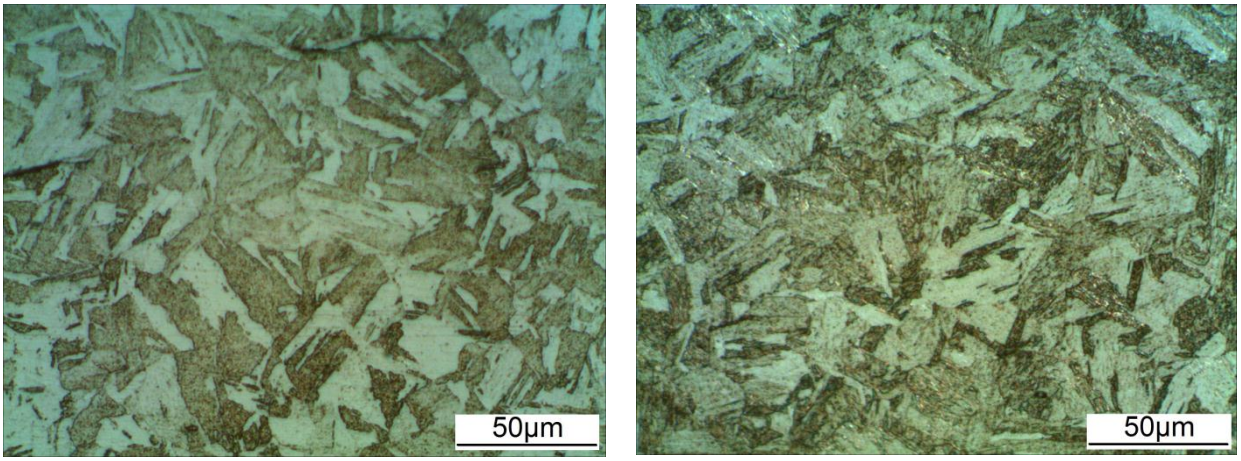

(a) (b)

Figure 16. Optical micrographs of (a) the solution annealed condition and (b) after aging for 2h at 500°C.

4.3. Nanoindentation

4.3.1. Solution annealed condition

Figure 17 illustrates one line of indentations on the solution annealed sample. Nanoindentation results show a significant hardness increase due to irradiation in the solution annealed material. The irradiated / unirradiated interface can be accurately measured using nanoindentation and agrees well with SRIM calculations, as shown in Figure 18. The blue curve illustrates the calculated damage profile and the red points represent the hardness values from nanoindentation. The low hardness values for the indentations close to the edge result from the extent of the plastic zone into the softer epoxy cold mount. In the irradiated area the hardness is about 6.7 GPa, compared to a hardness of about 5.6 GPa in the not irradiated material. Also the stopping peak, where

the material suffered a much higher damage and therefore the hardness increase is higher as well, is clearly detectable.

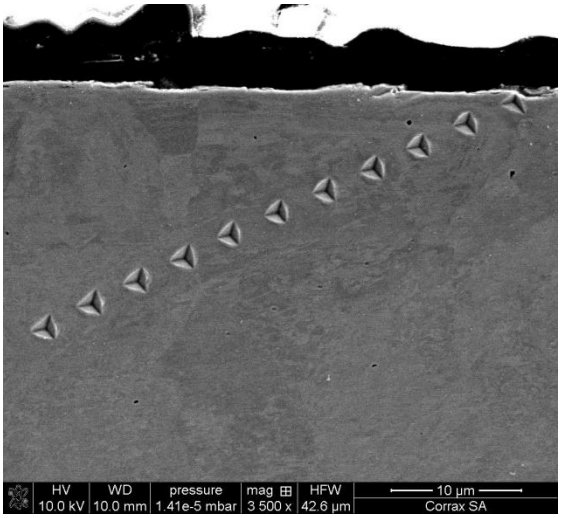

Figure 17. One line of indentations on the solution annealed sample.

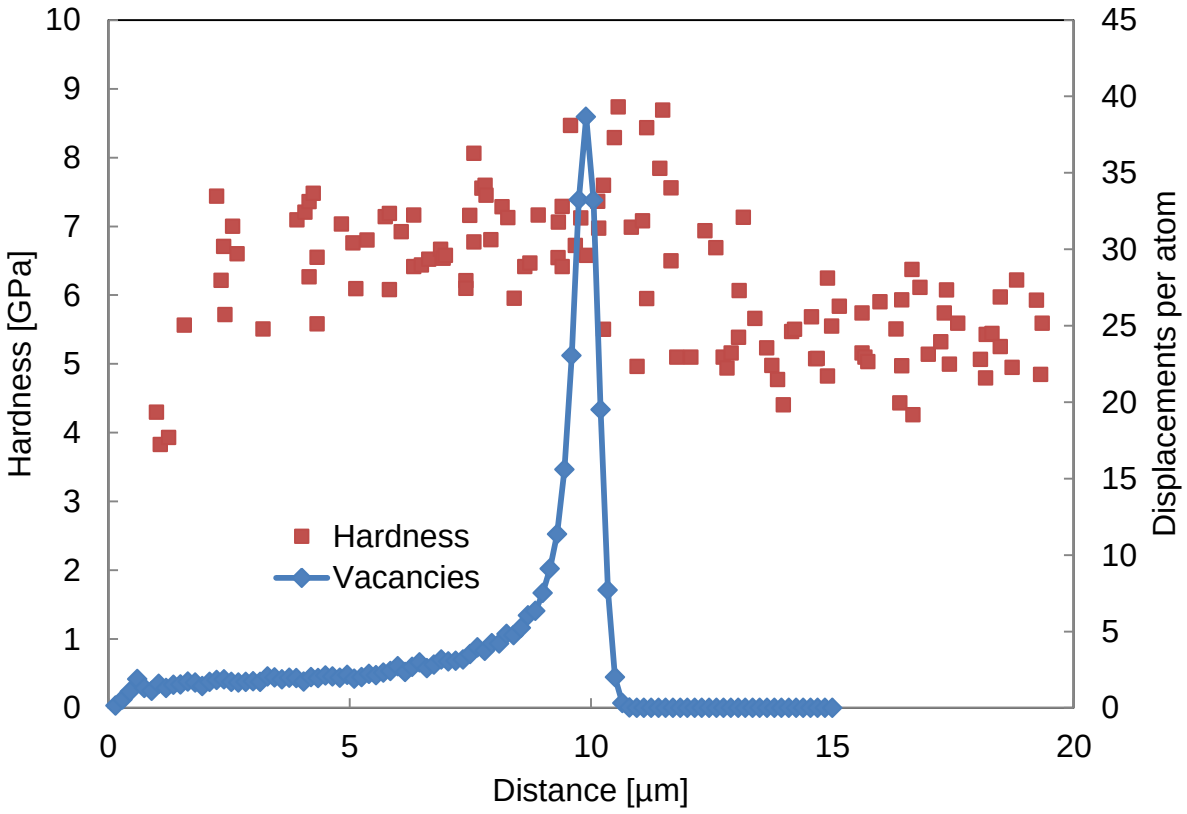

Figure 18. Hardness measured with nanoindentation and the calculated damage profile over the distance from the edge.

4.3.2. Aged condition

Figure 19 depicts the hardness profile measured on the sample aged for 2 h at 500°C. The hardness of the aged material is much higher due to precipitation hardening during aging compared to the solution annealed state. Irradiation only causes a very small increase in hardness of about 0.4 GPa.

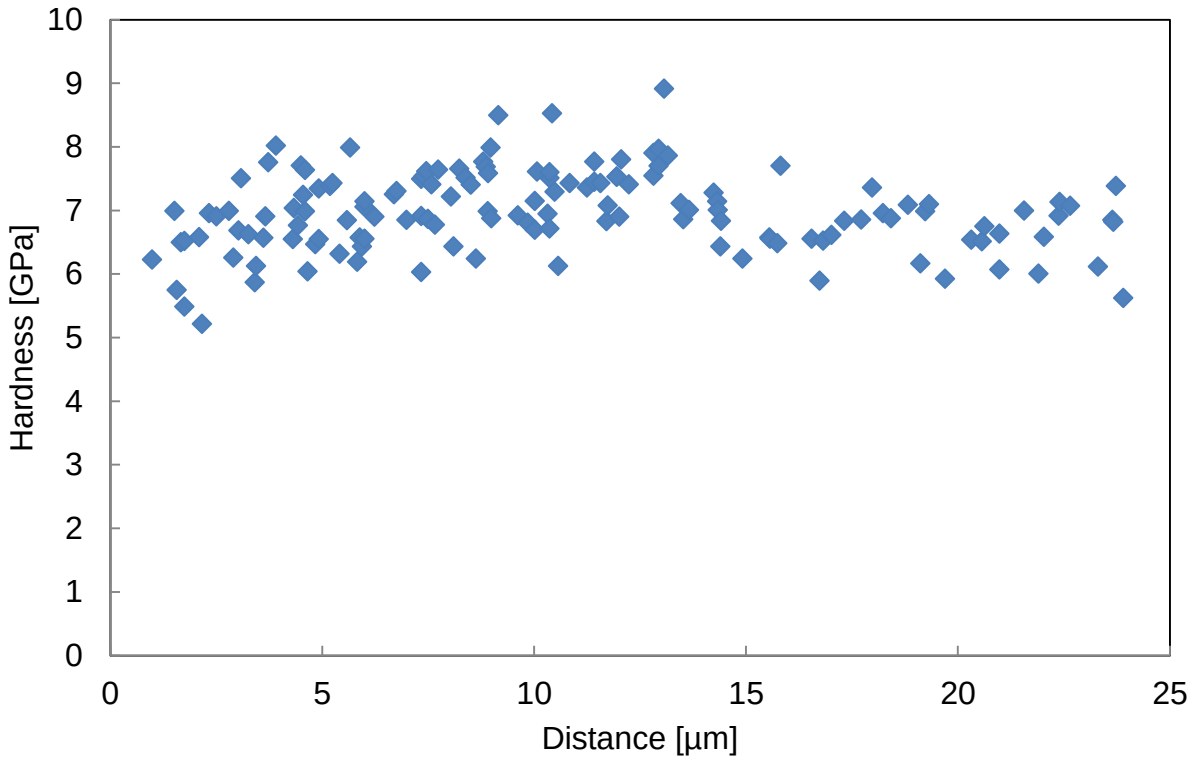

Figure 19. Hardness profile over the distance from the edge on the aged sample.

4.4. Atom probe tomography

4.4.1. Solution annealed condition

Atom maps of the solution annealed state are depicted in Figure 20. Through optical inspection of the three-dimensional reconstructions no clusters are found. This impression is confirmed by a frequency distribution (FD) analysis. If all atoms of one type of element are of random distribution the frequency distribution follows a binomial

model (21). A significant deviation of the binomial model indicates a non-random arrangement of the element.

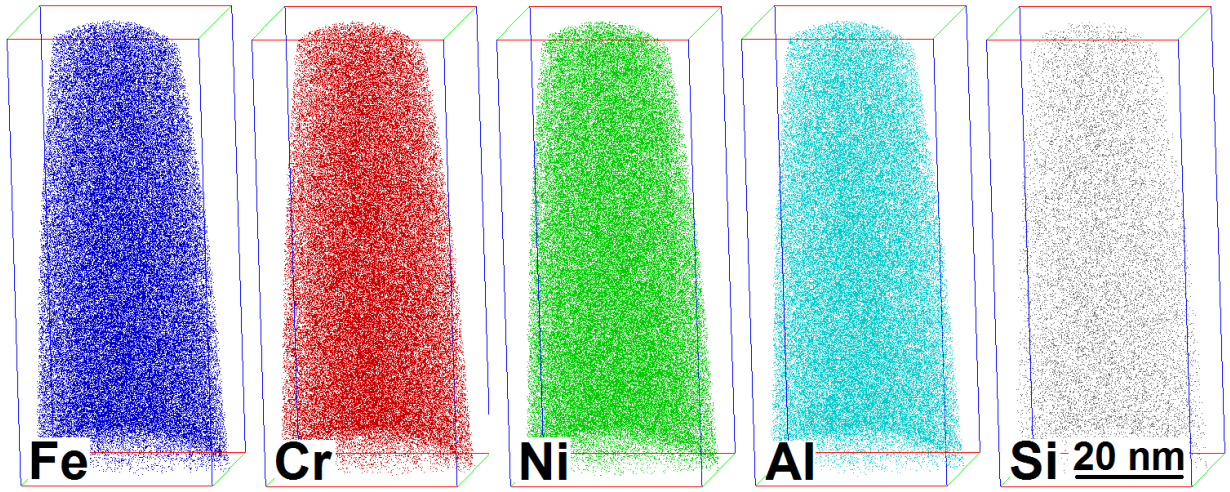

Figure 20. Atom maps of Fe, Cr, Ni, Al and Si the solution annealed state. There are no segregations visible.

4.4.2. Solution annealed and irradiated condition

The distribution of the elements seems to be homogeneous from visual inspection of the atom maps of Fe, Cr, Ni, Al and Si, shown in Figure 21. However, frequency distribution analysis reveals that all main elements are not randomly distributed. When phase separation occurs, the experimental concentration distribution deviates from the binomial distribution. FD results for Fe, Cr, Ni and Al are depicted in Figure 22. The deviation of the observed distribution from the binomial can be quantified by means of X^2 statistics (35):

$$X^2 = \sum_{n=0}^{n_b} \frac{(e(n) - f(n))^2}{f(n)}$$

where *e(n)* is the number of blocks containing *n* solute atoms measured experimentally and *f(n)* is the binomial distribution. Due to the fact that the X^2 test depends on the sample volume a parameter normalized to the number of blocks sampled, *N*, can be used:

$$\mu = \sqrt{\frac{X^2}{N + X^2}}$$

This parameter is called the Pearson coefficient and can range between 0 and 1, where 0 indicates a random distribution and 1 a complete decomposition of the solute atoms.

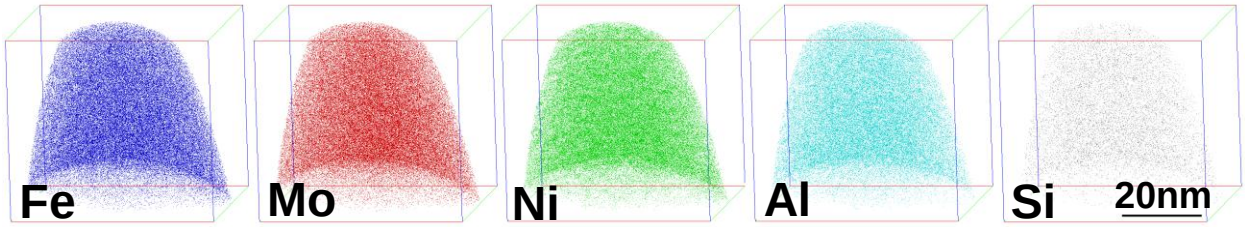

Figure 21. Atom probe maps of Fe, Cr, Si, Ni and Al of the solution annealed material after 2 dpa proton irradiation.

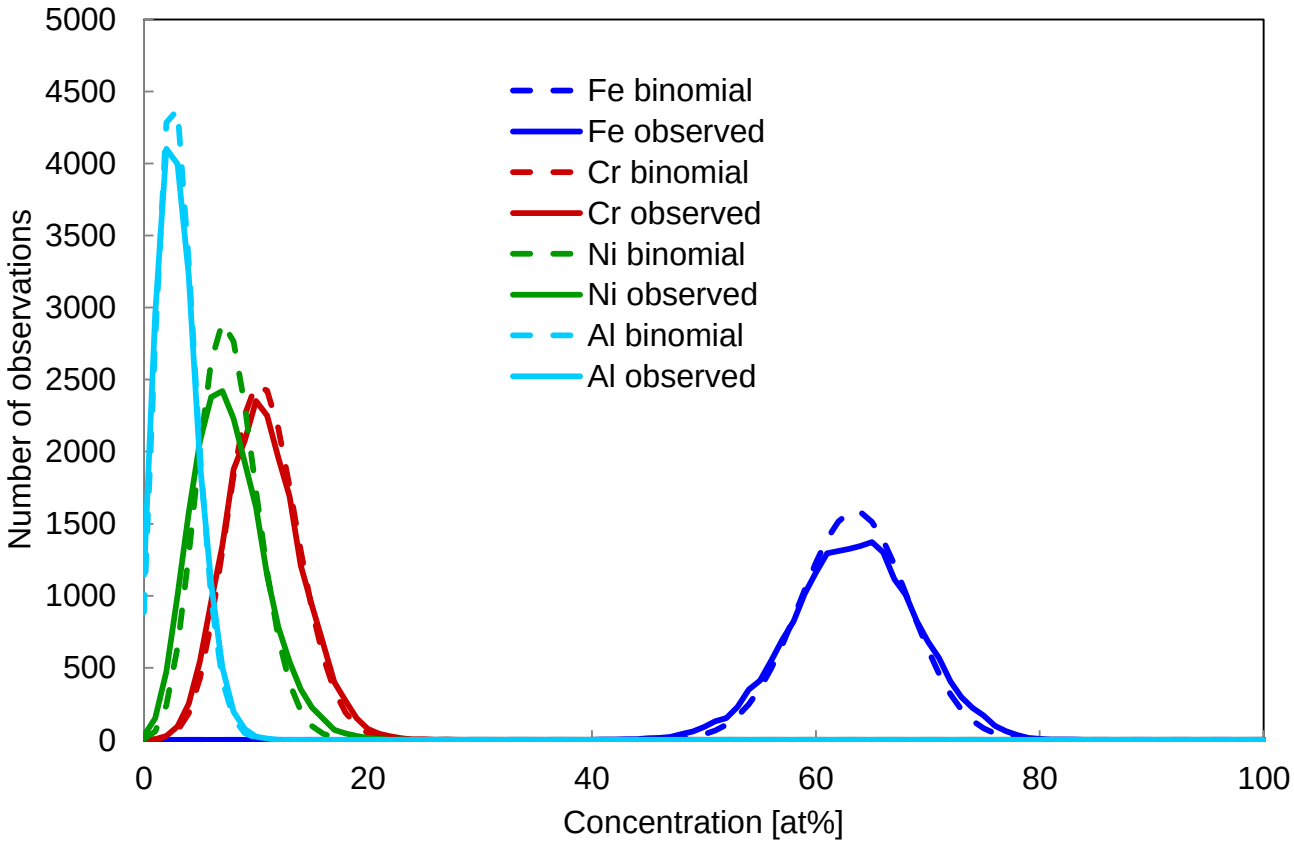

Figure 22. FD-Analysis of Fe, Cr, Ni and Al of the solution annealed sample. A decomposition of all phases is clearly evident.

High values for X^2 and μ imply decomposition of an element. As can be seen from Table 3 and Figure 22 especially Nickel indicates a considerable deviation from random distribution.

Table 3. Results from X^2 statistics of the irradiated solution annealed state.

	X^2	μ
Fe	36.47	0.24
Cr	16.33	0.13
Ni	139.58	0.34
Al	20.45	0.10
Si	22.56	0.07

A one-dimensional concentration profile through a cluster of Ni atoms was calculated according to the box in Figure 23. As illustrated in Figure 24, zones enriched with Ni and Si and depleted of Fe and Cr are measured.

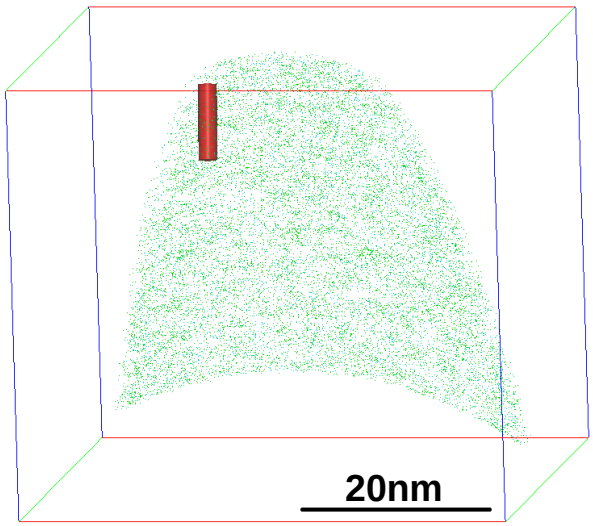

Figure 23. Analysis box through a Ni-enriched zone in the solution annealed and irradiated condition.

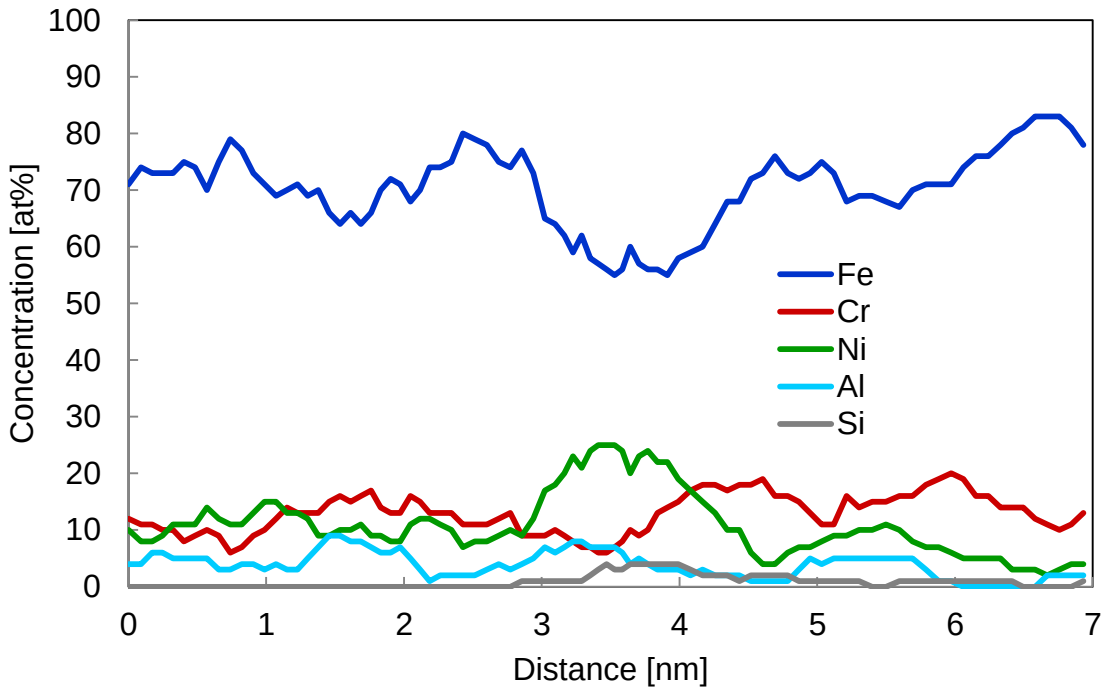

Figure 24. Concentration profile of the region of interest marked in Figure 23.

4.4.3. Aged condition

The sample aged for 2 h at 500°C displays precipitates enriched in Ni and Al, as depicted in Figure 25.

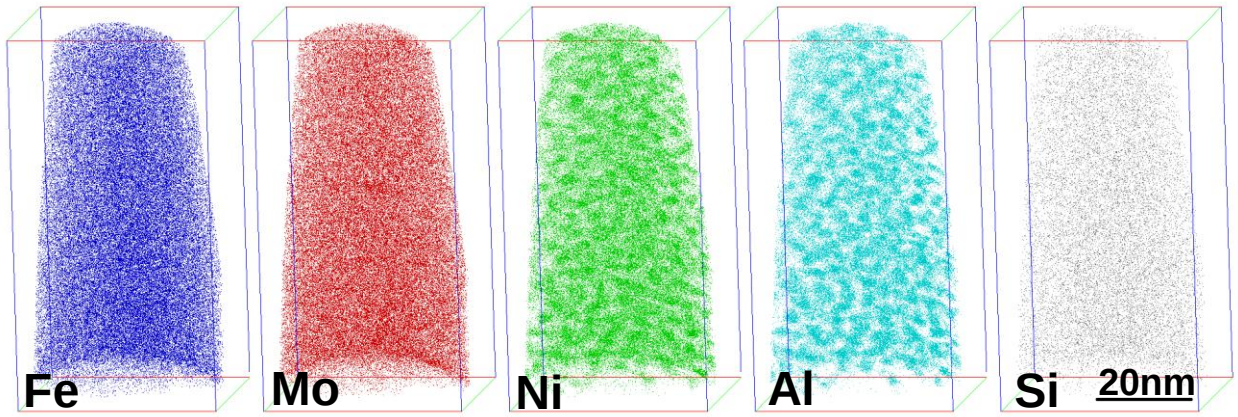

Figure 25. Atom probe maps of Fe, Cr, Ni, Al and Si of the material after aging for 2 h at 500°C.

A very useful tool to define solute-rich regions is a cluster search algorithm based on the maximum separation method (36). In this approach the simulation of a random distribution of atoms is compared to the actual distribution of the solute atoms. Based on that, a distance *d* is selected, which is the maximum distance between two solute atoms, belonging to the same particle. To make sure random accumulations of atoms are not included, a minimum number of solute atoms $N_{min,}$ is defined. This number is ascertained by plotting a size distribution for a simulated random distribution and then N_{min} set to the upper end of the distribution so only non-random clusters are part of the analysis. Once all solute atoms belonging to each particle have been detected, all non-solute atoms lying within a distance *L* around the cluster are also taken to be part of the particle. This last step distorts the composition of the clusters by including matrix atoms at the interface. Therefore, an erosion process to remove the outermost atoms is applied. Using the results of the cluster search, composition, size, shape, number density and volume fraction of the precipitates can be investigated.

For the aged sample d and L were set to 0.34 nm, the erosion distance was selected to be 0.17 nm and a minimum number of 27 ions was defined. The resulting clusters are illustrated in Figure 26 and the size distribution is depicted in Figure 27. The distribution is similar to a normal distribution and the precipitate sizes range from 0.4 nm to 1.3 nm. The average radius is 0.73 nm and the number density amounts to $7.5*10^{24}$ m^{-3}. Table 4 reveals the chemical composition of the precipitates and the matrix.

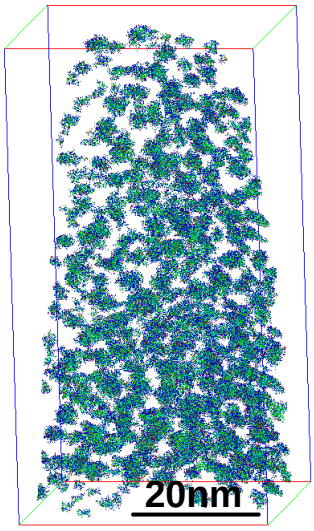

Figure 26. Cluster found by means of the cluster search algorithm in the material after aging for 2 h at 500°C.

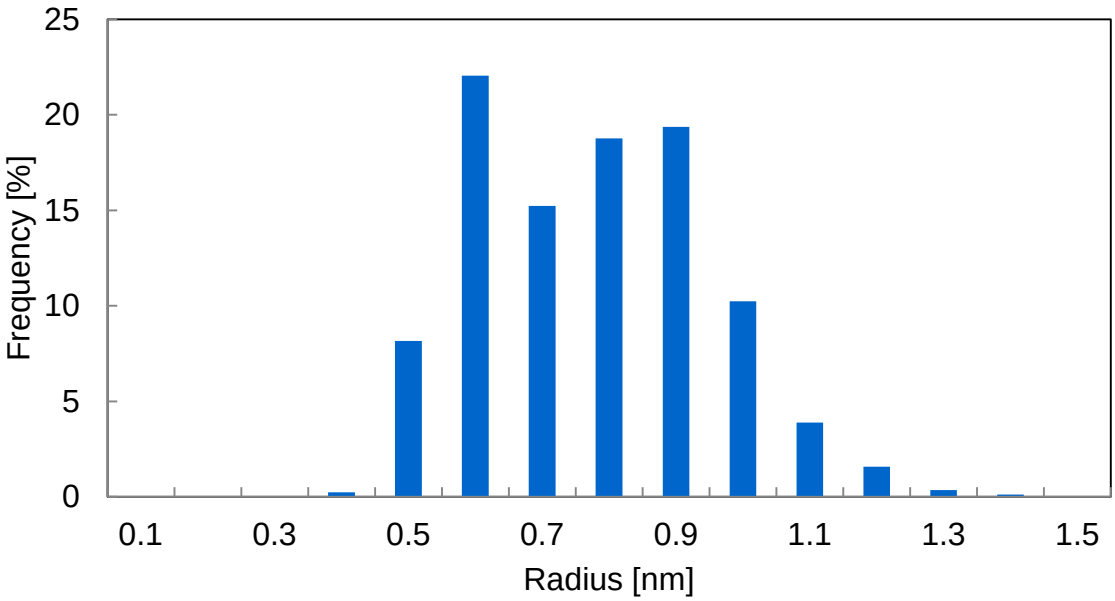

Figure 27. Size distribution of the precipitates after 2 h of aging at 500°C.

Table 4 reveals the chemical composition of the precipitates and the matrix. The errors on the concentration values are estimated by the standard deviation:

$$\sigma = \sqrt{\frac{c * (1 - c)}{N}}$$

where *c* is the measured concentration and *N* the total number of detected atoms. The bulk composition measured with the atom probe matches well with the nominal composition (Table 1). It can be seen that the particles are enriched with Ni, Al and Mn and on the other hand they are depleted of Fe and Cr. Correspondingly the matrix is depleted of Al and Ni. Nevertheless, the particles contain a high amount of Fe and are still far away from stoichiometric NiAl.

Table 4. Chemical composition in at% calculated with the cluster search algorithm for the aged sample.

	Fe	Cr	Ni	Al	Mo	Mn	Si	C
Bulk	Bal.	12.27 (±0.02)	8.76 (±0.02)	3.61 (±0.01)	0.76 (±0.01)	0.35 (±0.004)	0.65 (±0.005)	0.05 (±0.001)
Matrix	Bal.	13.04 (±0.02)	6.36 (±0.02)	1.91 (±0.01)	0.87 (±0.03)	0.26 (±0.003)	0.64 (±0.005)	0.06 (±0.001)
Precipitates	Bal.	6.66 (±0.05)	25.97 (±0.10)	15.84 (±0.08)	0.45 (±0.01)	1.02 (±0.02)	0.82 (±0.02)	0.05 (±0.004)

For better visualization of the shape of the precipitates isoconcentration surfaces (37) with a concentration threshold of 18 at% Ni+Al are depicted in Figure 28. A one-dimensional concentration profile according to the box of 2 nm x 2 nm x 6 nm in Figure 28 is shown in Figure 29.

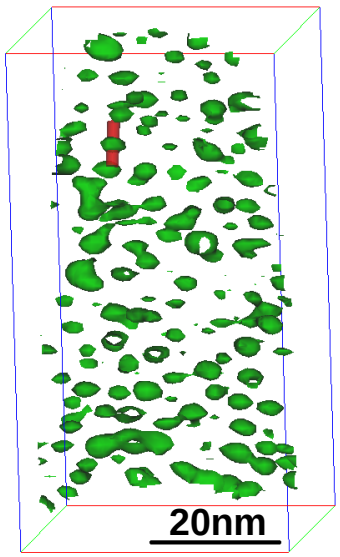

Figure 28. Analysis box through one precipitate.

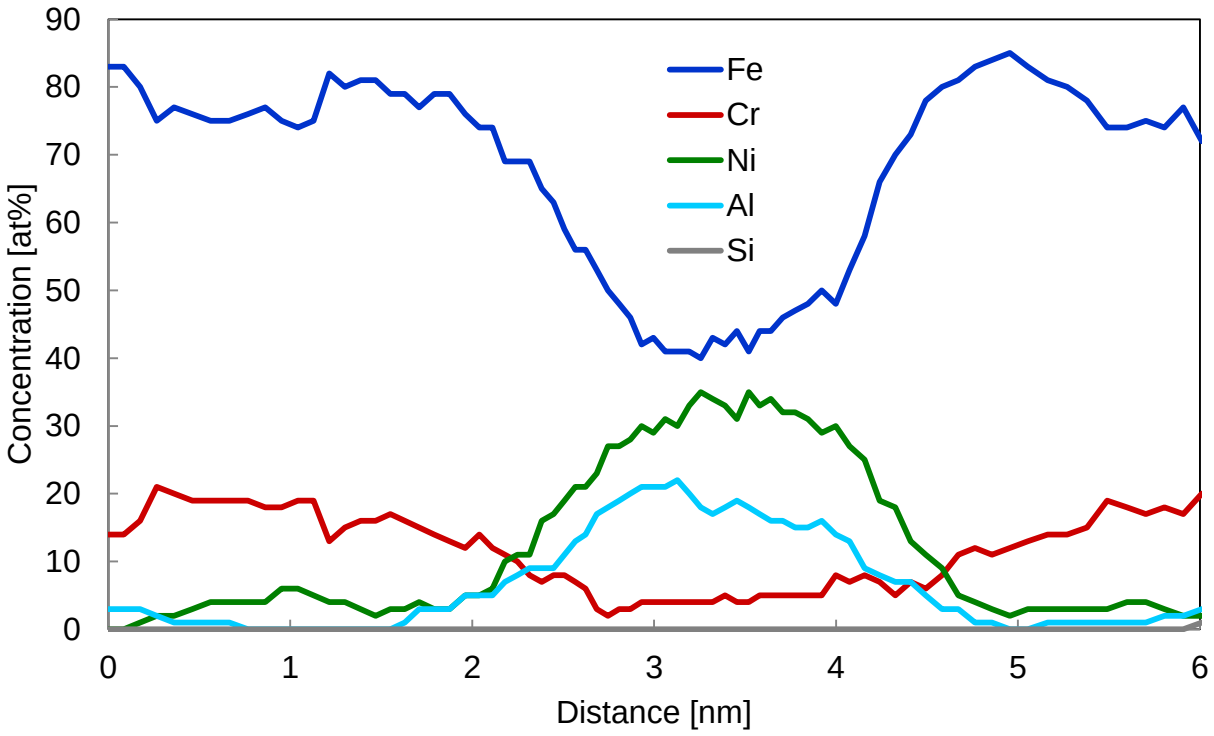

Figure 29. One-dimensional concentration profile across one precipitate as indicated in Figure 28.

4.4.4. Aged and irradiated condition

Figure 30 illustrates the atom maps of the material after aging for 2 h at 500°C and subsequent proton irradiation to 2 dpa. Again explicit precipitates are discernible.

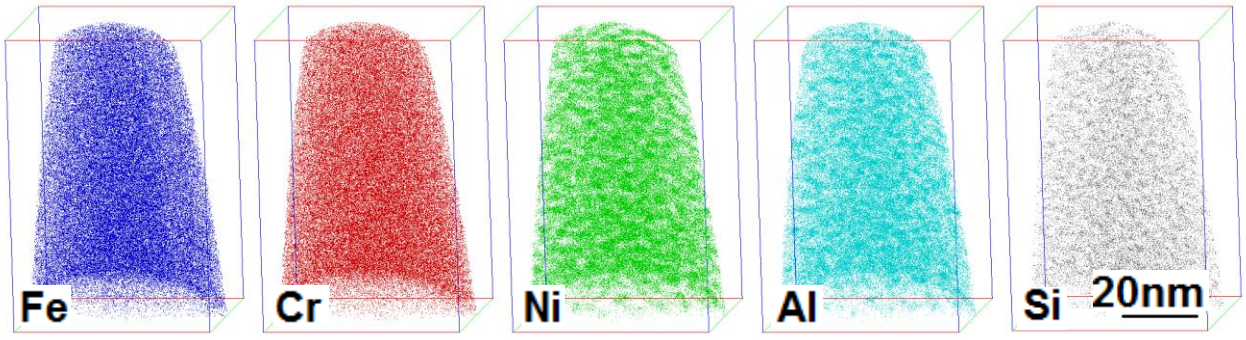

Figure 30. Atom maps of Fe, Cr, Ni, Al and Si after 2 h of aging at 500°C and 2 dpa proton irradiation.

When carrying out the cluster search on the aged and irradiated sample the parameters were set to d=0.34 nm, N_{min}=25, L=0.34 nm and l_{eros}=0.17 nm. Figure 31 displays the precipitates found by the cluster search algorithm.

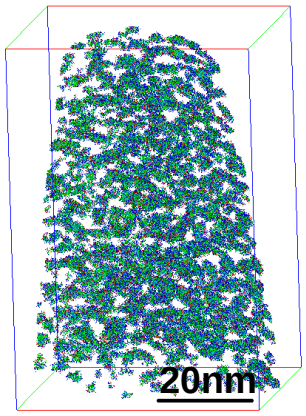

Figure 31. Precipitates in the aged and irradiated sample resulting from the cluster search algorithm.

Figure 32 shows the corresponding size distribution of the precipitates in the aged and irradiated sample. The precipitates have an average radius of 0.72 nm and a number density of $7.6*10^{24}$ m^{-3}.

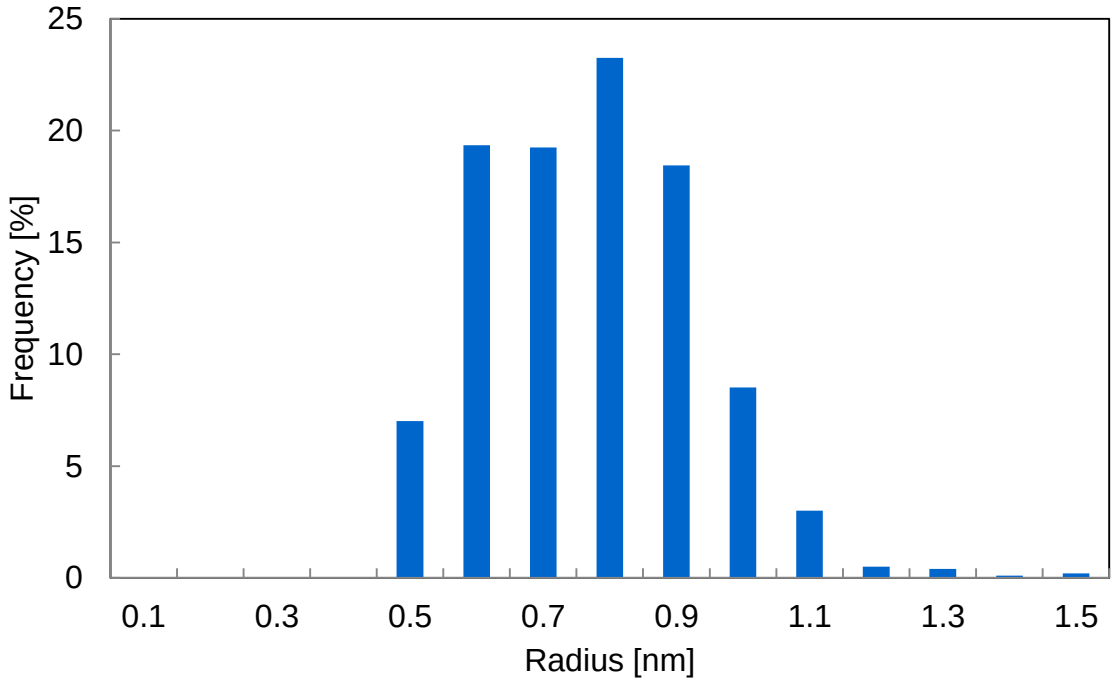

Figure 32. Size distribution of the precipitates in the aged and irradiated specimen.

The chemical composition of the precipitates and the matrix is given in Table 5. The precipitates are enriched with Ni, Al and Si, and depleted of Fe and Cr. Again, there is still a significant amount of Fe in the precipitates.

Table 5. Chemical composition in at% calculated with the cluster search algorithm for the aged and irradiated sample.

	Fe	Cr	Ni	Al	Mo	Mn	Si	C
Bulk	Bal.	12.4 (±0.02)	8.98 (±0.02)	3.69 (±0.01)	0.82 (±0.005)	0.37 (±0.003)	0.66 (±0.004)	0.02 (±0.001)
Matrix	Bal.	13.05 (±0.02)	6.69 (±0.01)	2.71 (±0.01)	0.92 (±0.005)	0.34 (±0.003)	0.51 (±0.004)	0.03 (±0.001)
Precipitates	Bal.	7.29 (±0.02)	27.26 (±0.04)	10.73 (±0.03)	0.34 (±0.004)	0.56 (±0.006)	2.06 (±0.01)	0.02 (±0.001)

Figure 33 displays isoconcentration surfaces for a threshold of 18 at% Ni+Al and the concentration profile through one precipitate according to the analysis box is presented in Figure 34.

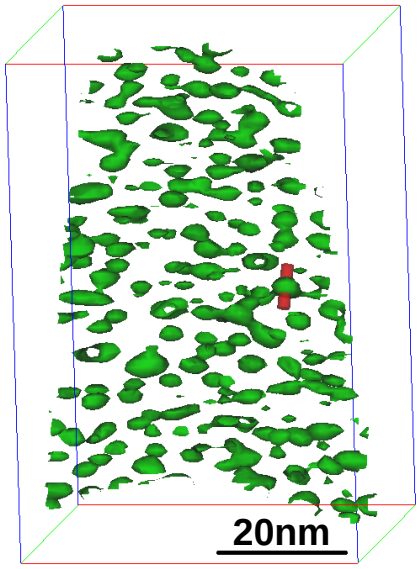

Figure 33. Analysis box through one precipitate.

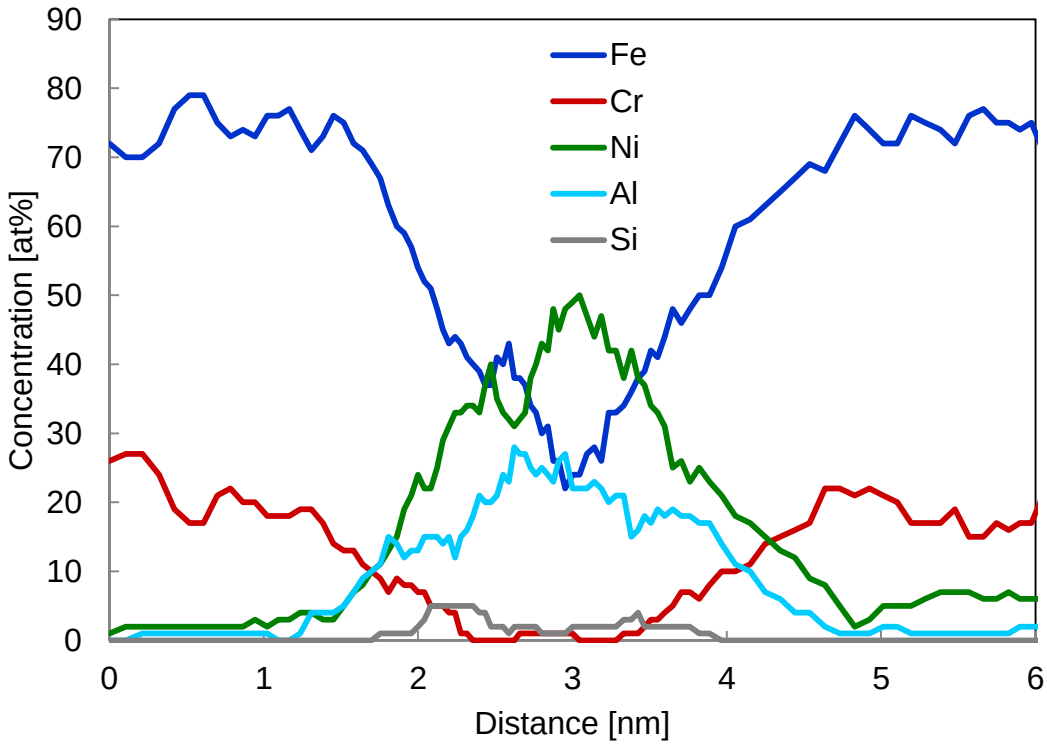

Figure 34. Concentration profile of the region of interest marked in Figure 33.

Based on the isoconcentration surfaces it is possible to calculate a proximity histogram (38), which shows the concentration over the proximity normal to the isosurfaces. Figure 35 depicts the comparison of the concentration of the aged sample before and after irradiation. The concentration of Ni and Si increases in the precipitates during irradiation, whereas the concentration of Al decreases.

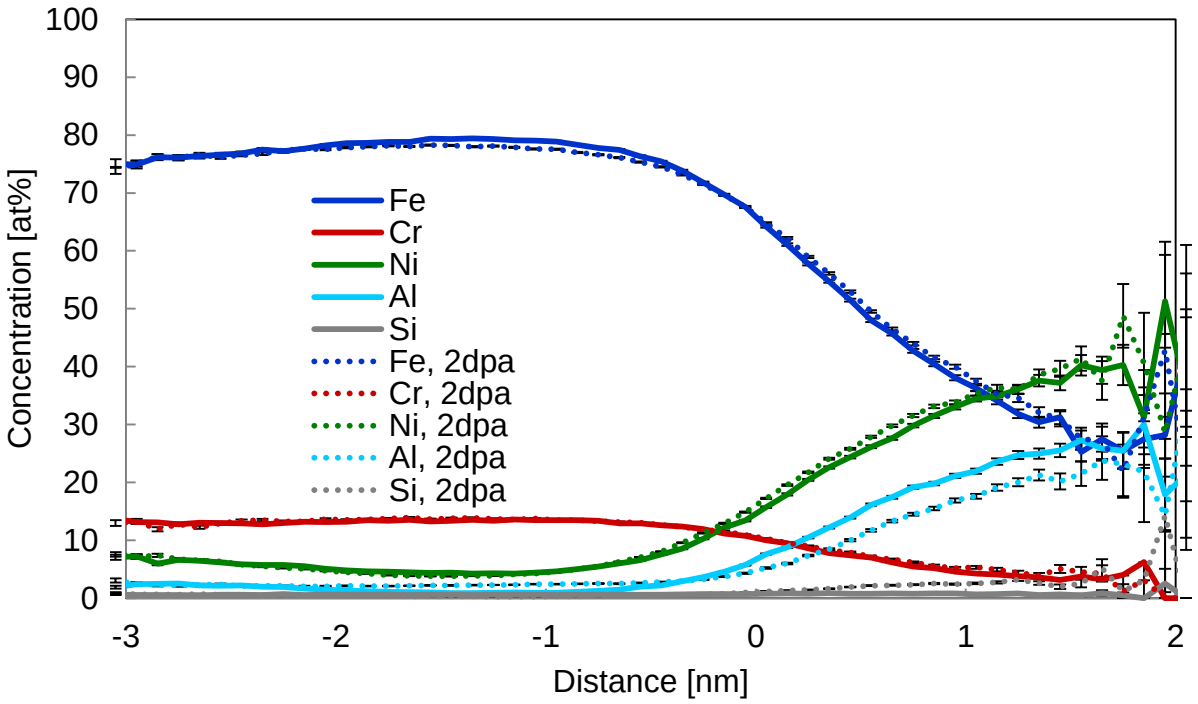

Figure 35. Proximity histogram of Fe, Cr, Ni, Al and Si for an isoconcentration threshold of 18 at% Ni+Al. The continuous lines corresponds to the unirradiated, the dotted line to irradiated material.

4.5. Micro-compression testing

Micro-compression tests were performed on the solution annealed sample. The dimensions of the pillars were obtained with the scanning electron microscope prior to testing and are summarized in Table 6. The distance from the edge was measured from the interface specimen/ epoxy cold mount to the center of the pillar. SEM pictures were acquired ante and post testing. Pillar 2 in the unirradiated area and Pillar 1 in the irradiated area are exemplarily depicted in Figure 36.

Table 6. Dimensions of the micro-pillars, measured in the SEM.

	d_1 (µm)	d_2 (µm)	A (µm^2)	Height (µm)	Distance from the edge
Pillar 1, not irr.	10.0	10.0	100.00	14.22	-
Pillar 2, not irr.	9.5	6.1	57.95	12.00	-
Pillar 3, not irr.	7.8	6.0	46.80	13.10	-
Pillar 1, irr.	11.4	6.5	74.10	20.65	2.7
Pillar 2, irr.	10.7	6.1	65.27	20.65	4.1
Pillar 3, irr.	8.5	4	34.00	15.40	6.8

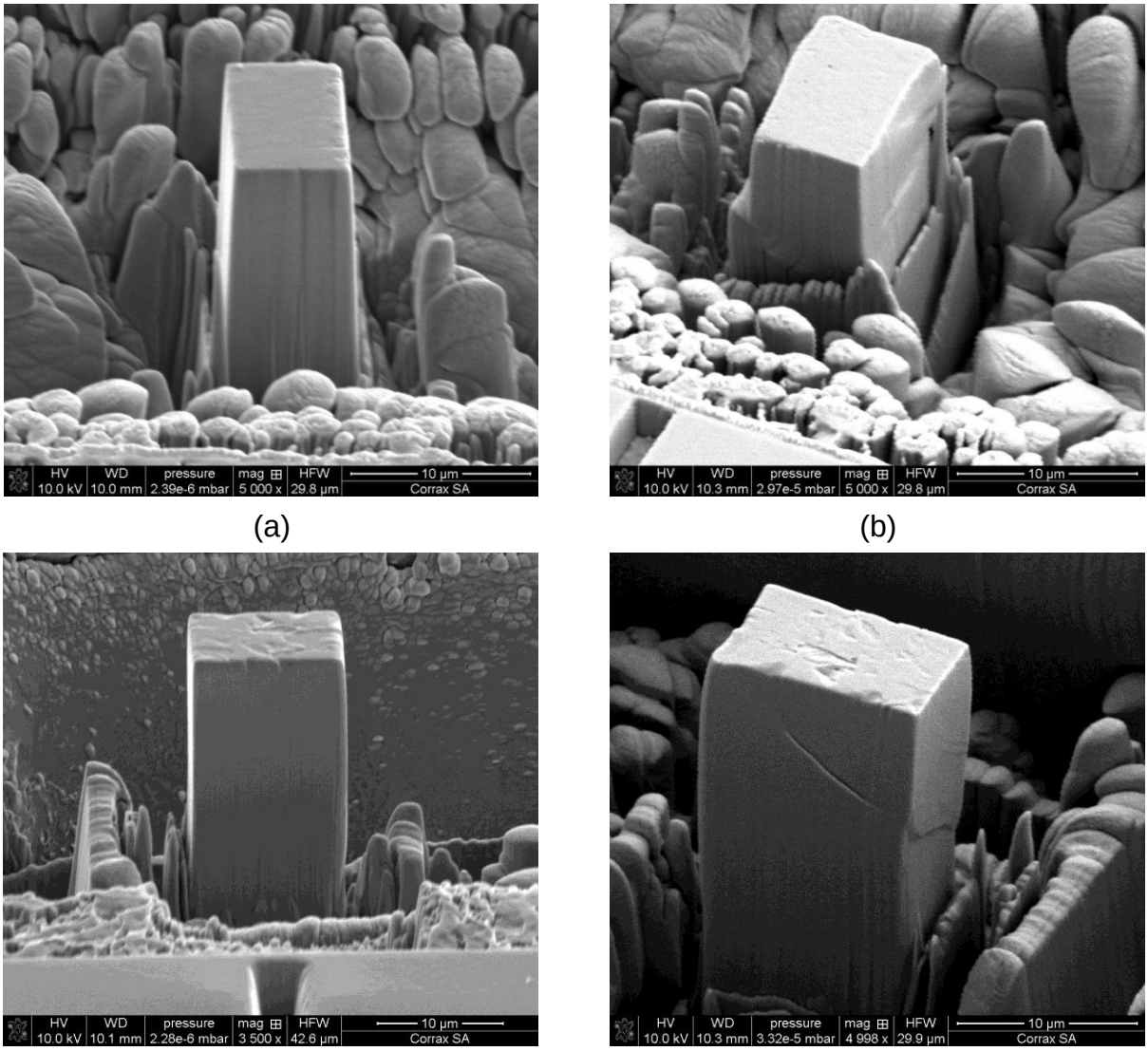

(a) (b)

(c) (d)

Figure 36. Pillar 2 in the unirradiated area (a) ante and (b) post testing and Pillar 1 in the irradiated area (c) ante and (d) post testing.

Figure 37 illustrates the engineering stress-strain curves for the unirradiated material.

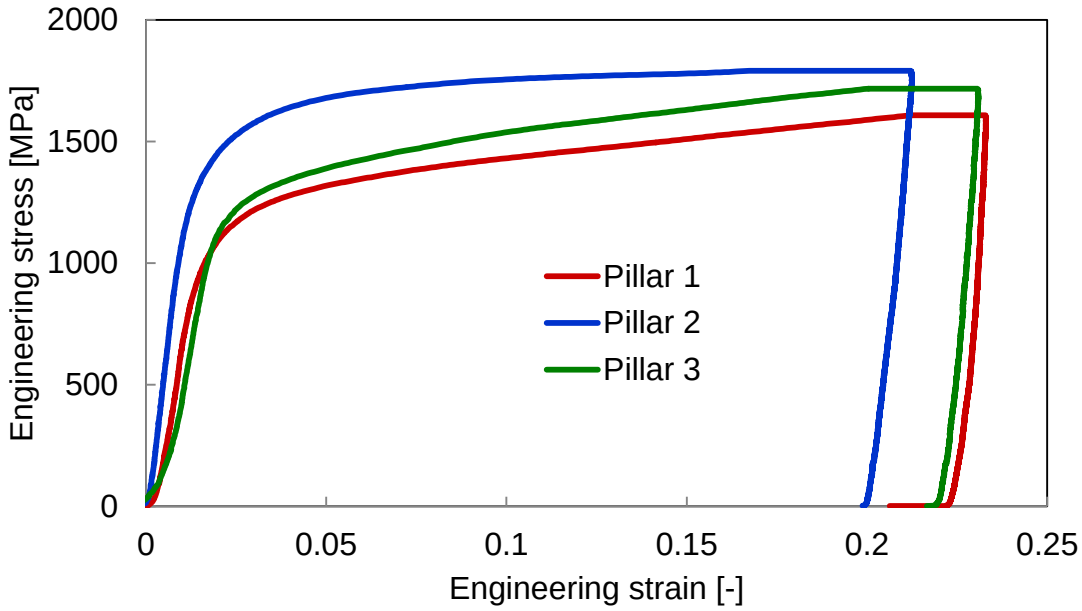

Figure 37. Stress-strain curves gained from micro-compression tests on PH 13-8 Mo in the solution annealed state on the not irradiated part.

Figure 38 shows the pillars in the irradiated area post testing. Pillar three did not work out and the results could not be used. The red line indicates the interface to the epoxy cold mount. Pillar 1 and 2 are close to the edge, but pillar 4 is at the distance of the stopping peak and suffered a much higher dose rate.

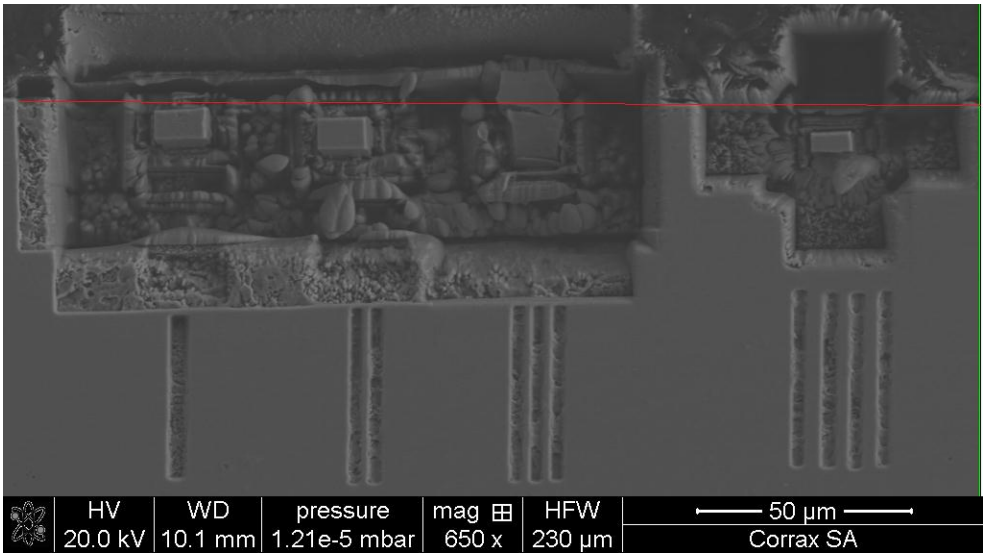

Figure 38. Top view of the pillars in the irradiated area post testing. The red line indicates the interface to the epoxy cold mount.

Engineering stress-strain curves for the pillars in the irradiated area are illustrated in Figure 39. Due to the fact that pillar 4 is located at the stopping peak, where the radiation damage is much higher, the increase in yield strength is more pronounced compared to pillar one and two.

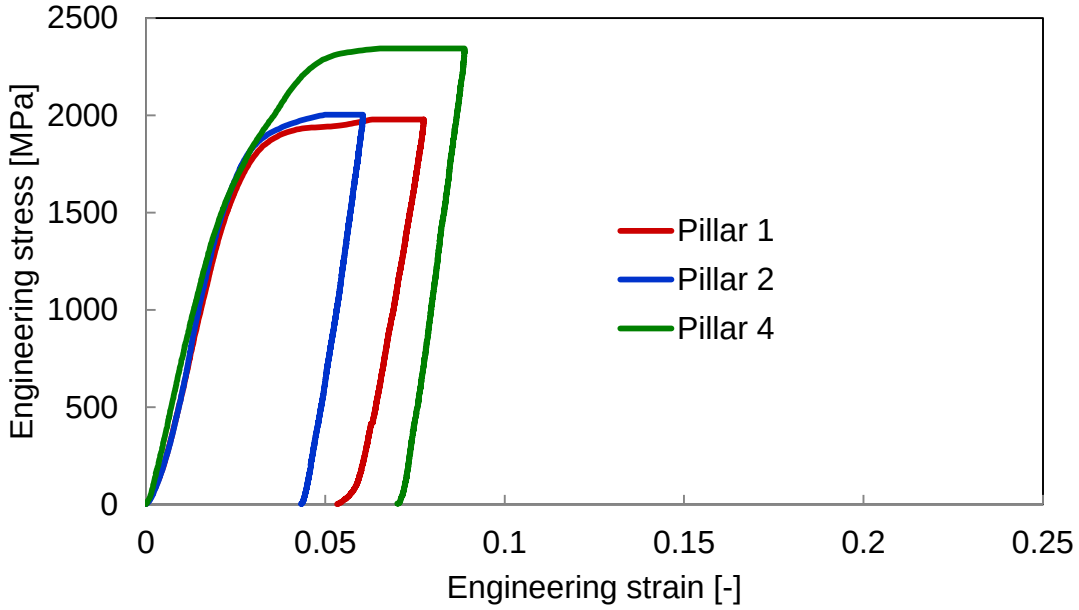

Figure 39. Engineering stress-strain curves gained from micro-compression tests on the irradiated area of the solution annealed sample.

0.2% offset yield strength was measured for each pillar by parallel movement of the linear part of the loading curve by 0.002 of the engineering strain. This minimizes the influence of contact misfits occurring at the initial stage of loading. Results from the micro-compression tests are given in Table 7. The $R_{p0.2}$ value of pillar 4 underestimates the increase in strength because a deviation of the linear-elastic line around 1700 MPa occurs and therefore the offset yield strength cannot be accurately measured.

Table 7. 0.2% offset yield strength of the micro pillars.

	Distance from the edge [µm]	$R_{c0.2}$ [N/mm^2]
Pillar 1, unirr.	-	990
Pillar 2, unirr.	-	1260
Pillar 3, unirr.	-	1160
Pillar 1, irr.	5.9	1660
Pillar 2, irr.	7.6	1730
Pillar 4, irr.	8.8	1650

5. Discussion

Comparison of the solution annealed condition and the condition aged for 2 h at 500°C before and after irradiation showed distinct differences in the material behavior.

5.2. Solution annealed condition

Examination of the solution annealed and irradiated material in the atom probe showed non-random distribution of all main elements. The Pearson coefficient *μ* revealed that especially Nickel is decomposed. A one-dimensional concentration profile through a cluster of Ni atoms, as shown in Figure 24, revealed zones enriched with Ni and Si and depleted of Fe and Cr.

An explanation for the decomposition could be radiation-enhanced diffusion. During irradiation a large number of point defects are generated. The stimulated diffusion can lead to defect aggregation or precipitation, depending on the balance between defect production rate and the loss of point defects to recombination or sinks (12).

The energy input during heat treatment also leads to a higher mobility of atoms due to an increase in the vacancy concentration. As a result to the enhanced diffusion precipitates are able to develop from the supersaturated solid solution (39).

In this work an attempt was made to calculate a diffusion coefficient during irradiation and set into proportion to the diffusion coefficient during aging.

5.2.1. Aging at 500°C

The vacancy concentration during heat treatment results from the free vacancy formation energy G_f^v, the Boltzmann constant *k*, and the aging temperature *T*:

$$C_v = exp^{(\frac{-G_f^v}{kT})}$$

The free vacancy formation energy was taken to be 1.4 eV, the energy for vacancy formation in α-Fe (40). The diffusion coefficient depends on the number of nearest neighbors *z*, the diffusion mechanism and the crystal structure, both considered in the parameter *A*, the lattice constant a_0, and the jump frequency ω:

$$D_v = \alpha * a_0^2 * \omega$$

with

$$\alpha = \frac{1}{6} * z * A^2$$

The jump frequency is the frequency with which an atom tries to break down the potential barrier between two equilibrium positions, generally assumed as the Debye frequency $v_D \approx 10^{13} s^{-1}$ multiplied with the Boltzmann factor, which takes into account the probability of success:

$$\omega = \nu * exp^{\left(\frac{S_m^v}{kT}\right)} * exp^{\left(\frac{-E_m^v}{kT}\right)}$$

The vacancy migration entropy can be neglected and therefore, the diffusion coefficient results in:

$$D_v = \alpha * a_0^2 * \nu * exp^{\left(\frac{-E_m^v}{kT}\right)}$$

with a vacancy migration energy of 0.68 eV (12). The diffusion coefficient of lattice atoms by way of the vacancy mechanism is given by:

$$D_a = D_v C_v$$

For a body-centered material aged at 500°C for 2 h the diffusion coefficient accounts for $2.27*10^{16}$ cm^2/s. This result agrees well with the diffusion coefficient for Fe in Fe diffusion of 10^{16} cm^2/s in the literature (39).

5.2.2. Irradiation

During irradiation not only vacancies but also a large amount of interstitials are created. The behavior of these radiation-induced point defects depends on a large part on the amount of sinks in the material. A great number of sinks accomplishes that interstitials get caught in sinks before they have a chance to recombine with vacancies. Hence,

after the point defect built-up, the concentration of vacancies C_v, increases, while the interstitial concentration C_i, decreases until both reach a quasi-steady state (Figure 40) (12):

$$c_v^{SS} = -\frac{K_{is}C_s}{2 * K_{iv}} + [\frac{K_0 K_{is}}{K_{iv}K_{vs}} + \frac{K_{is}^2 C_s^2}{4 * K_{iv}^2}]^{\frac{1}{2}}$$

$$c_i^{SS} = -\frac{K_{vs}C_s}{2 * K_{iv}} + [\frac{K_0 K_{vs}}{K_{iv}K_{is}} + \frac{K_{vs}^2 C_s^2}{4 * K_{iv}^2}]^{\frac{1}{2}}$$

where

C_s = sink concentration

K_0 = defect production rate

K_{iv} = vacancy-interstitial recombination rate coefficient

K_{vs} = vacancy-sink reaction rate coefficient

K_{is} = interstitial-sink reaction rate coefficient

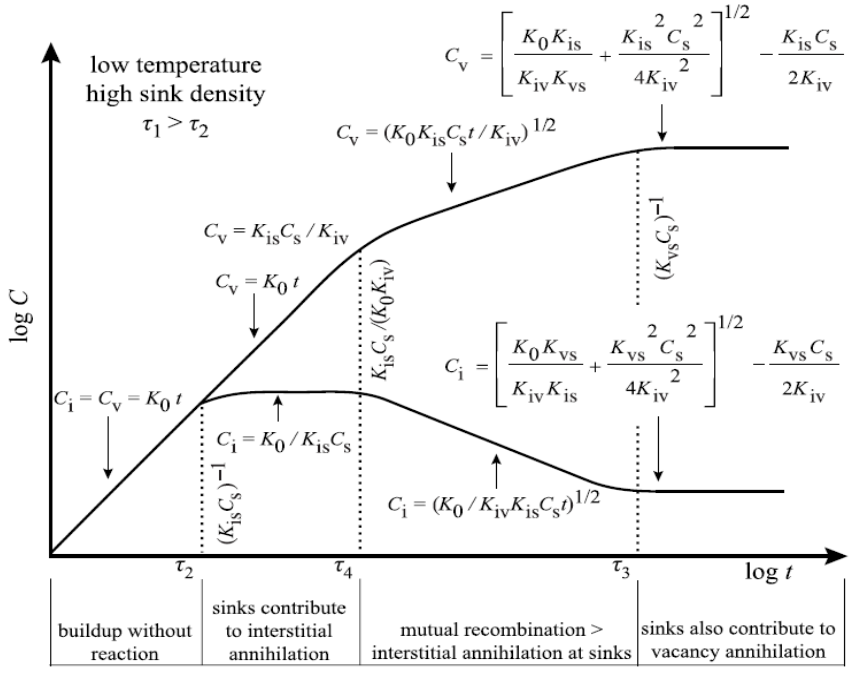

Figure 40. Vacancy and interstitial concentration plotted over the time for irradiation at room temperature and a high sink density (41).

The vacancy production rate $K_{0,}$ is obtained from the SRIM calculation and amounts to 2.5*10^{18} vac/cm^3*s. The most important sinks in PH 13-8 Mo are dislocations and therefore, the dislocation density ρ_D=10^{12} m^{-2} (42), is part of the equation for the sink concentration:

$$C_s = \frac{\rho_D}{a_0}$$

The interstitials and vacancies migrate by random walk diffusion, annihilating each other by mutual recombination or at unsaturable fixed sinks. Sinks and defects are distributed homogeneously and no preferential absorption of specific point defects at specific sinks occurs. Therefore, the rate constants are as follows:

$$K_{iv} \approx 4 * \pi * r_{iv} * D_i$$

$$K_{is} = 4 * \pi * r_{is} * D_i$$

$$K_{vs} = 4 * \pi * r_{vs} * D_v$$

where r_{iv}, r_{vs} and r_{is} are interaction radii for the reaction between the species. R_{vs} and r_{is} were taken to be equal to the lattice parameter a_0, and r_{iv} is about twice as much (43). The diffusion coefficient for interstitials is calculated the same way as for vacancies:

$$\mathrm{D_i} = \alpha * \mathrm{a_0^2} * \nu * \exp^{(\frac{-\mathrm{E_m^i}}{\mathrm{kT}})}$$

with an interstitial migration energy of 0.33 eV (12).

The diffusion coefficient of lattice atoms is obtained with the same equation as before, but this time, the diffusion caused by interstitials also needs to be considered:

$$\mathrm{D_a} = \mathrm{D_v C_v} + \mathrm{D_i C_i}$$

The diffusion coefficient during irradiation added up to 3.21*10^{18} cm^2/s and is about two orders of magnitude lower than the diffusion coefficient during aging at 500°C.

This agrees well with the results obtained in the atom probe and explains why only decomposition and not full precipitation took place.

Accompanied with the decomposition the hardness increased substantially. Guo et al. (8) also observed hardening effects during the initial stage of aging before detectable precipitates formed. They attributed this increase in hardness to the redistribution of

atoms. Reich et al. (44) suggested a solute-dislocation interaction, where solute atoms segregate to existing dislocation causing dislocation locking.

Besides the decomposition also radiation-induced defects affect the hardness. The large amounts of vacancies and interstitials created during radiation can evolve to larger defects, e.g. dislocation loops (12). Dislocation loops act as dispersed barriers for dislocation glide and therefore increase the yield strength. Transmission electron microscopy (TEM) examination would be necessary to visualize them; however, this would exceed the extent of this work.

In order to estimate the increase in yield strength by nanoindentation, the correlation proposed by Busby et al. (45) was applied:

$$\Delta\sigma_y = 3.06 * \Delta H_v$$

ΔH_v is the increase in Vickers hardness in kg/mm^2 and $\Delta\sigma_y$ is the consequential increase in yield strength. The conversion of the hardness increase measured with nanoindentation into Vickers hardness was performed according to (15). Pillar 4 in the irradiated material was excluded of the calculation because of its different radiation dose. Table 8 summarizes the changes in hardness and yield strength.

Table 8. Increase in yield strength due to irradiation on the solution annealed sample.

Measured ΔH (nanoindentation)	Calculated ΔH_v	Calculated $\Delta\sigma_y$ (Busby)	Measured $\Delta\sigma_y$ (micropillars)
1.14 GPa	107.4 kg/mm^2	329 MPa	558 MPa

The difference between the calculated yield strength increase, based on the nanoindenation measurements, and the experimentally observed one, gained from pillar tests, can have a variety of reasons. The irradiated and unirradiated material exhibits a different indentation size effect because of their different intrinsic hardness (20). Micro-compression tests were designed for single crystals and the influence of the different orientations of the martensitic laths was not taken into account. Misalignment has a strong impact on the test accuracy, leading to a smearing of the transition from elastic-to-plastic deformation. Also detrimental effects arise from dust particles on the sample or the flat-punch indentation tip, plastic buckling of the pillar and gallium implementation due to the fabrication in the FIB (32).

5.3. Aged condition

Nanoindentation only revealed a very small increase in hardness due to irradiation in the sample aged at 500°C for 2 h. The precipitates formed during the aging treatment delayed the radiation damage. The large amount of defect sinks, such as dislocations and grain boundaries, capture the point defects produced during the radiation process.

Van Renterghem et al. (46) suggested that existing precipitates are not influenced by radiation because number density and radius do not change during irradiation. They attributed the hardness increase to the formation of dislocation loops. In this work, radius and number density are also comparable before and after irradiation, but the composition of the precipitates changes during the irradiation process. The proximity histogram in Figure 35 revealed that the Al concentration decreased while the Si concentration increased in the precipitates due to irradiation. This might indicate that a change of precipitate type takes place which has a larger solubility for Si (47). The interaction of radiation and precipitates is very complex. Further studies are required to make a more precise statement.

6. Summary

In this work the influence of proton irradiation on the precipitation kinetics and the resulting changes in mechanical properties of a PH13-8Mo maraging steel were investigated by means of nanoindentation, micro-pillar testing and atom probe tomography.

The nanoindentation results showed that in the solution annealed state a distinct hardness increase of 1.1 GPa due to irradiation occurred. Atom probe tomography revealed a decomposition of the main elements and zones enriched with Ni and Si were detected. This can be explained by the enhanced diffusion due to an increased amount of vacancies and interstitials produced during irradiation. In this work an attempt was made to calculate a diffusion coefficient during irradiation and set into proportion to the diffusion coefficient during aging. It turned out that the diffusion coefficient during irradiation is about two orders of magnitude lower than during aging at 500°C explaining why decomposition and not full precipitation occurred. The decomposed regions in combination with radiation induced defects such as dislocation loops are most likely responsible for the increase in hardness. Micro-compression tests also confirmed the increase in yield strength and correlate quite well with the estimation from nanoindentation.

As expected, the material aged for 2 h at 500°C only exhibited a small hardness increase of about 0.4 GPa. The large amount of defect sinks diminished the degradation of the material under irradiation. The number density and the radius are comparable before and after irradiation but the composition of the precipitate changes. It seems that a new precipitation type containing Ni, Al and Si developed. Further studies are required to make a more precise statement.

References

1. **Was, G.S. et al.** Emulation of neutron irradiation effects with protons: validation of principle. *Journal of Nuclear Materials.* 2002, 300, pp. 198-216.

2. **G. Odette, M. Alinger, B. Wirth.** Recent Developments in Irradiation-Resistant Steels. *Annual Review of Materials Research.* 2008, Vol. 38, pp. 471-503.

3. **Gelles, D.S. et al.** Microstructural examination of commercial ferritic alloys at 200 dpa. *Journal of Nuclear Materials.* 1996, Vols. 233-237, pp. 293-298.

4. **Zot'ev, Y.A. et al.** Radiation Resistance of Maraging Steel. *Metallovedenie i Termicheskaya Obrabotka Metallov.* 1974, Vol. 10, pp. 43-45.

5. **V. Seetharaman, M. Sundararaman, R. Krishnan.** Precipitation Hardening in a PH 13-8 Mo Stainless Steel. *Materials Science and Engineering.* 1981, Vol. 47, pp. 1-11.

6. **R. Taillard, A. Pineau.** Room Temperature Tensile Properties of Fe-19wt.%Cr Alloys Precipitation Hardened by the Intermetallic Compound NiAl. *Materials Science and Engineering.* 1982, Vol. 56, pp. 219-231.

7. **Schnitzer, R.** *Structure-Properties Relationship of a Stainless Maraging Steel.* 2010.

8. **Z. Guo, W. Sha, D. Vaumousse.** Microstructural evolution in a PH13-8 stainless steel after aging. *Acta Materialia.* 2003, Vol. 51, pp. 101-116.

9. **M. Schober, R. Schnitzer, H. Leitner.** Precipitation evolution in a Ti-free and Ti-containing stainless maraging steel. *Ultramicroscopy.* 2009, Vol. 109, pp. 553-562.

10. **R. Taillard, A. Pineau, B.J. Thomas.** The Precipitation of the Intermetallic Compound NiAl in Fe-19wt.%Cr Alloys. *Materials Science and Engineering.* 1982, Vol. 54, pp. 209-219.

11. **D.H. Ping, M. Ohnuma, Y. Hirakawa, Y. Kadoya, K. Hono.** Microstructural evolution in 13Cr-8Ni-2.5Mo-2Al martensitic precipitation-hardened stainless steel. *Materials Science and Engineering A.* 2005, Vol. 394, pp. 285-295.

12. **Was, G.S.** *Fundamentals of Radiation Materials Science.* Heidelberg : Springer Verlag Berlin, 2007.

13. **W.C. Oliver, G.M. Pharr.** Measurement of hardness and elastic modulus by instrumented indentation: Advances in understanding and refinements to methodology. *Journal of Materials Research.* 2004, Vol. 19, 1.

14. **D.A. Lucca, K. Herrmann, M.J. Klopfstein.** Nanoindentation: Measuring methods and applications. *CIRP Annals - Manufacturing Technology.* 2010, Vol. 59, pp. 803-819.

15. *Correlation of Nanoindentation and Conventional Mechanical Property.* **P.M. Rice, R.E. Stoller.** Materials Research Society Symposium Proceeding : s.n., 2000.

16. **W.C. Oliver, G.M. Pharr.** An improved technique for determining hardness and elastic modulus using load and displacement sensing indentation experiments. *Journal of Materials Research.* 1992, Vol. 7, 6, pp. 1564-1583.

17. **M.F. Doerner, W.D. Nix.** A method of interpreting the data from depth-sensing indentation instruments. *Journal of Materials Research.* 1986, Vol. 1, pp. 601-609.

18. **Fischer-Cripps, A.C.** *The IBIS Handbook of Nanoindentation.* Forestville : Fischer-Cripps Laboratories Pty Ltd., 2005.

19. *The role of indentation depth on the measured hardness of materials.* **De Guzman, M.S. et al.** Materials Research Society Symposium Proceedings : s.n., 1993. Vol. 308, pp. 613-618.

20. **W.D. Nix, H. Gao.** Indentation size effects in crystalline materials: A law for strain gradient plasticity. *Journal of the Mechanics and Physics of Solids.* 1998, Vol. 46, 3, pp. 411-425.

21. **M.K. Miller, R.G. Forbes.** Atom probe tomography. *Materials Characterization.* 2009, 60, pp. 461-469.

22. **J.F. Ziegler, J.P. Biersack, U. Littmark.** *The Stopping and Range of Ions in Matter, SRIM.* New York : Pergamon, 1985.

23. **G.H. Pease, R.S. Kinchin.** The Displacement of Atoms in Soldis by Radation. *Reports on Progress in Physics.* 1955, 18, pp. 1-51.

24. *http://www.lanl.gov/mst/docs/LALP-06-036.pdf.*: LANL, August 2011.

25.*http://www.werc.or.jp/english/reseadeve/activities/accelerator/accelerator/tandem/index.htm.*: The Wakasa Wan Energy Research Center, August 2011.

26. **Hosemann, P. et al.** Nanoindentation on ion irradiated steel. *Journal of Nuclear Materials.* 2009, Vol. 389, pp. 239-247.

27. **B.D. Beake, S.R. Goodes, J.F. Smith.** Nanoscale materials testing under industrially relevant conditions: high-temperature nanoindentation testing. *Zeitschrift für Metallkunde.* 2003, Vol. 94, pp. 798-801.

28. **Miller, M.K.** *Atom probe tomography.* New York : Springer, 2000.

29. **M.K. Miller, K.F. Russell, K. Thompson, R. Alvis, D.J. Larson.** Review of Atom Probe FIB-Based Specimen Preparation Methods. *Microscopy and Microanalysis.* 2007, Vol. 13, pp. 428-436.

30. **M.K. Miller, K.F. Russell.** Atom probe specimen preparation with a dual beam SEM/FIB miller. *Ultramicroscopy.* 2007, Vol. 107, pp. 761-766.

31. **Hosemann, P. et al.** Macro and microscale mechanical testing and local electrode atom probe measurements of STIP irradiated F82H, Fe-8Cr ODS and Fe-8Cr-2W ODS. *Journal of Nuclear Materials.* 2011. in press.

32. **M.D. Uchic, D.M. Dimiduk.** A methodology to investigate size scale effects in crystalline plasticity using uniaxial compression testing. *Materials Science and Engineering A.* 2005, 400-401, pp. 268-278.

33. **Sneddon, I.N.** The relation between load and penetration in the axisymmetric bussinesq problem for a punch of abitrary profile. *International Journal of Engineering Science.* 1965, Vol. 3, pp. 47-57.

34. **C.A. Volkert, E.T. Lilleodden.** Size effects in the deformation of sub-micron Au columns. *Philosophical Magazine.* 2005, Vol. 86, pp. 5567-5579.

35. **Moody, P. et al.** Quantitative Binomial Distribution Analyses of Nanoscale Like-Solute Atom Clustering and Segregation in Atom Probe Tomography Data. *Microscopy Research and Technique.* 2008, Vol. 71, pp. 542-550.

36. **V. Vaumousse, A. Cerezo, P.J. Warren.** A procedure for quantification of precipitate microstructures from three-dimensional atom probe data. *Ultramicroscopy.* 2003, Vol. 95, pp. 215-221.

37. **O.C. Hellman, J. Blatz du Rivage, D.N. Seidman.** Efficient sampling for three-dimensional atom probe microscopy data. *Ultramicroscopy.* 2003, Vol. 95, pp. 199-205.

38. **O.C. Hellman, J.A. Vandenbroucke, J. Rüsing, D. Isheim, D.N. Seidman.** Analysis of Three-dimensional Atom-probe Data by the Proximity Histogram. *Microscopy and Microanalysis.* 2000, Vol. 6, pp. 437-444.

39. **Gottstein, G.** *Physikalische Grundlagen der Materialkunde.* s.l. : Springer-Verlag Berlin Heidelberg, 2007.

40. **S.M. Kim, W.J.L. Buyers.** Vacancy formation energy in iron by positron annihilation. *Metal Physics.* 1987, Vol. 8.

41. **Sizemann, R.** *Journal of Nuclear Materials.* 1987, Vol. 69/70, pp. 386-412.

42. **E.V. Pereloma, A. Shekhter, M.K. Miller, S.P. Ringer.** Ageing behaviour of an Fe-20Ni-1.8Mn-1.6Ti-0.59Al (wt%) maraging alloy: clustering, precipitation and hardening. *Acta Materialia.* 2004, Vol. 52, pp. 5589-5602.

43. **Macht, M.P. et al.** Temperature-Dependent Sink Concentration in Ni and Cu. *Physica Status Solidi A.* 1987, Vol. 104, pp. 287-295.

44. **L. Reich, S.P. Ringer, K. Hono.** Origin of the initial rapid age hardening in an Al-1.7 at.% Mg-1.1 at.% Cu alloy. *Philosophical Magazine Letters.* 1999, Vol. 9, 79, pp. 639-648.

45. **Busby, J.T. et al.** The relationship between hardness and yield stress in irradiated austenitic and ferritic steels. *Journal of Nuclear Materials.* 2005, 336, pp. 267-278.

46. **W. Van Renterghem, A. Al Mazouzi, S. Van den Berghe.** Defect structure of irradiated PH13-8Mo steel. *Journal of Nuclear Materials.* 2007, Vol. 360, pp. 128-135.

47. **Raghavan, V.** Al-Ni-Si (Aluminium-Nickel-Silicon). *Journal of Phase Equilibria and Diffusion.* 2005, Vol. 26, 3, pp. 262-267.